Earth Science Data Records of Global Forest Cover and Change

User Guide

Sexton, JO [a*], M Feng [a], S Channan [a], X-P Song [a], D-H Kim [a], P Noojipady [a], D Song [a], C Huang[a], A Annand [a], K Collins [a], EF Vermote [b], R Wolfe [c], J Masek [b], JRG Townshend [a†]

[a] The Global Land Cover Facility, Department of Geographical Sciences, University of Maryland, College Park, MD 20740

[b] Biospheric Sciences Branch, NASA Goddard Space Flight Center, Greenbelt, MD 20771, USA

[c] Laboratory for Terrestrial Physics, NASA Goddard Space Flight Center, Greenbelt, MD 20771, USA

*Corresponding author: jsexton@umd.edu

†Principal Investigator: jtownshend@umd.edu

1. Introduction

1.1. Background

Changes in the Earth's forest cover impact the water, energy, carbon, and other nutrient cycles, as well as the ability of ecosystems to support biodiversity and human economies. Knowledge of the patterns and rates of forest-cover change is critical to understand the causes and effects of land-use change (Band 1993; Lal 1995; Houghton 1998; Pandey 2002) and to manage ecosystems sustainably. A number of national and international programs have called for routine monitoring of global forest changes, including the Global Observation for Forest and Land Cover Dynamics (GOFC-GOLD) (Skole *et al.* 1998; Townshend *et al.* 2004), Global Climate Observing System (GCOS 2004), and the U.S. Global Change Research Program (USGCRP 1999). An examination of the societal benefits defined by the Group on Earth Observations and the Strategic US Integrated Earth Observation System revealed that resolutions to all of these issues are dependent on regular and reliable land cover change monitoring (Townshend & Brady 2006).

Coarsely scaled measurements of the Earth's forest cover have been produced at regional and national extents (Skole and Tucker 1993, Tucker and Townshend 2000, Steininger et al. 2001, DeFries et al. 2002, Zhang et al. 2005, Huang et al. 2007). However, most of these representations are static; and although a substantial proportion of change has been shown to occur at resolutions below 250 m (Townshend & Justice 1988), global assessments of forest cover and its changes at high-resolution are still in nascent stages of development while local and regional products (e.g., Lepers et al. 2005) lack consistency and comparability. Relying on national inputs and sampled remotely sensed data, the United Nations Food and Agriculture Organization (FAO) Forest Resource Assessment (FRA) carried out limited Landsat-based sampling of change detection to assist the estimation of global tropical forest change rates for 1990-2000 (FAO 2001). However, these sample-based assessments provide inadequate quantitative information on the distribution of change (Matthews and Grainger 2002, DeFries et al., 2002). Landsat-class resolutions are essential for detecting fine-scale changes, particularly those resulting from local anthropogenic factors.

1.2. Objective

The objective of this project was to provide a multi-temporal forest cover Earth Science Data Record (ESDR) at global extent and "Landsat" (30 m) and "MODIS" (250, 500, 1000 m, 0.05°) resolutions. Requirements for such products are specified in many documents, including the *ESDR Community White Paper on Land Cover/Land Change* (Masek et al. 2006a) and the *Global Observations of Forest Cover/Land-Cover Dynamics (GOFC-GOLD) Fine-Resolution* design documents (Skole *et al.* 1998, Townshend *et al.* 2004). This record includes:

- Global 30 m resolution estimates of surface reflectance for four epochs:1990, 2000, 2005, and 2010 derived from the Global Land Survey (GLS)
- Global 30 m resolution forest cover and change (FCC) estimates from 1990 to 2000, and 2000 to 2005 with per-pixel level accuracy indicators

- Global 250 m, 500 m, 1 km, and 0.05° gridded FCC ESDR products aggregated from the 30 m resolution FCC product.
- Tree Cover Product
- Water Mask

1.3. Approach

Global, spatially and temporally comprehensive forest cover and change Earth Science Data Records were produced from 30 m and 250 m resolution satellite data. At 30 m spatial resolution, forest cover and changes in and between 1990, 2000, and 2005 were mapped using the enhanced Global Land Survey (GLS+) data sets, supplemented with additional images where and when the GLS data were incomplete or inadequate for analysis (Tucker et al. 2004, Gutman et al. 2008, Channan et al. 2015). This effort also included production of surface reflectance ESDRs at 30 m resolution for 1990, 2000, 2005, and 2010. (Note that the years 1990, 2000, 2005, and 2010 for all fine-resolution data sets refer to nominal years, but the actual acquisition year of the GLS+ data set varies from place to place due to cloud cover and image availability).

The fine-resolution ESDRs were produced using algorithms that have been implemented or are now implemented in the Landsat Ecosystem Disturbance Adaptive Processing System (LEDAPS), which was developed through previous NASA projects and includes algorithms for geometric orthorectification, radiometric normalization, and data quality screening. Atmospherically corrected surface reflectance, which is the basis for many other ESDRs and analyses, was generated as an intermediate product. Products to quantify and monitor fragmentation were also generated. Efforts were restricted to mapping per-pixel gains and losses of forest cover between the epochs at fine spatial resolution and between years for moderate spatial resolution. Also, the definition of FCC was restricted exclusively to changes in forest *cover* and not to any change in the type of forest *land use* (cf. FRA 2000). Like any ESDR, the data produced contain uncertainty, but this 15-year record represents a major advance in our understanding of the Earth’s changing forest cover. In processing the fine- and moderate-resolution data sets, we ensured that the data provide coverage of the greatest extent possible, are internally consistent, and that errors and uncertainty are thoroughly characterized.

1.4. Significance

These Earth Science Data Records provide the first and only consistent, global record of forest cover changes documenting the period from 1990 to 2005, and they enable the first comprehensive assessment of Earth’s forest cover at a scale appropriate to recent changes. The data also provide the basis for understanding impacts of forest change on the Earth system, including carbon budgets and the hydrological cycle. The moderate-resolution products are of particular value to various modeling communities, especially those concerned with regional to global carbon modeling (Ojima & Galvin 1994, et al. 1999) and regional hydrological modeling (Band 1993, Sahin & Hall 1996, Bounoua et al., 2002). The fine resolution products supports habitat analyses and other ecological studies at scales ranging from local to global, which is particularly valuable to natural resource managers, especially those responsible for conserving biodiversity (Dudley et al. 2005; Hilli & Kuitunen 2005). The protected area subsets of the forest change and fragmentation records allow assessment of local conservation efforts as well as the broader effectiveness of international environmental and biodiversity agreements.

2. Methodology

2.1. Input Data

2.1.1. Global Land Survey

The primary data source for generating the fine resolution ESDRs were the GLS Landsat image datasets centered around 1990, 2000, and 2005. The GLS is a partnership between USGS and NASA, in support of the U.S. Climate Change Science Program and the NASA Land-Cover and Land-use Change (LCLUC) Program. Building on the existing GeoCover dataset developed for the 1970s, 1990, and 2000 (Tucker et al. 2004), the GLS was selected to provide wall-to-wall, orthorectified, cloud free Landsat coverage of Earth's land area at 30- meter resolution in nominal “epochs” of 1990, 2000, and 2005 (Franks et al. 2009, Gutman et al. 2008). The GLS was intended to provide one clear-view image acquired during the peak growing season of each epoch for each World Reference System (WRS) scene. The 1990 epoch ranges from 1984 to 1997 and is composed of 7,375 Landsat-5 Thematic Mapper (TM) images. The GLS 2000 is composed of 8,756 Landsat-7 Enhanced Thematic Mapper Plus (ETM+) images from 1999 to 2002. The GLS 2005 is composed of 7,284 gap-filled Landsat-7 ETM+ images and 2,424 Landsat-5 TM images acquired between 2003 and 2008. In many cases, however, images had to be selected with a date outside this range, mostly due to lack of cloud-free images during the growing season (Franks et al. 2009, Gutman et al. 2008, Channan et al. 2015). Because images have been selected from somewhat different dates, there are variations in phenology which account for the patchiness of image mosaics in some locations (Kim et al. 2011; Townshend et al. 2012).

The original GLS data set did not fully cover the Earth’s terrestrial surface in all epochs; gap were filled to the highest degree possible with newly available images. No data exist to fill an expansive coverage gap over central and eastern Siberia in the 1990 epoch. Smaller, isolated holes also persist where coverage is missing in one or several adjacent WRS tiles for individual epochs; we obtained the best available Landsat images to fill these gaps. Finally, GLS images acquired near or during the leaf-off season, which are not suitable for forest cover change analysis, were replaced with images acquired during the local “leaf-on” growing season to use in our forest cover change analysis, pending availability (Kim et al. 2011, Channan et al. 2015).

A challenge in using GLS data sets for analysis is that many of the GLS images were acquired near or during leaf-off seasons. Because the spectral differences between leaf-on and leaf-off deciduous forests can be great, automated FCC analysis based on leaf-off images can result in widespread, erroneous changes. Prior to classification and forest change analysis, each Landsat image was evaluated to determine its phenological suitability for forest cover change analysis. We used the NDVI temporal profiles calculated using the Global Inventory Modeling and Mapping Studies (GIMMS) Advanced Very High Resolution Radiometer (AVHRR) and the Moderate Resolution Imaging Spectroradiometer (MODIS) data record (Tucker et al., 2005) to determine whether an image was acquired near or during leaf-off seasons. The GLS 1990, 2000, and 2005 images were evaluated using the GIMMS record directly.

Many non-GLS Landsat images were needed to supplement the GLS dataset to produce the fine resolution ESDR products. We developed and implemented an orthorectification algorithm in the LEDAPS software that automatically orthorectifies a Landsat image to match the GLS dataset (Gao et al. 2009). During extensive validation, residual misregistration errors in the orthorectified products were found to be less than one pixel.

The GLCF (www.landcover.org) currently houses and distributes the GLS Landsat dataset for the 1975, 1990, 2000, 2005 and 2010 epochs. Depending on the epoch, approximately 7–10,000 Landsat scenes have been compiled to cover the global land area (Gutman et al. 2013; Feng et al. 2013).

2.1.2. Digital Elevation Model: ASTER GDEM (v2.0)

We used the Global Digital Elevation Model, version 2.0 (GDEM v2.0) as an ancillary layer in many analyses. Produced from images acquired by the Advanced Spaceborne Thermal Emission and Reflection Radiometer (ASTER) the GDEM dataset was jointly released by the Ministry of Economy, Trade, and Industry (METI) of Japan and NASA. The 30-meter resolution `ASTER GDEM was generated using stereo-pair images collected by the ASTER instrument onboard the Terra satellite. ASTER GDEM v2.0 data from the Land Processes Distributed Active Archive Center's (LP DAAC) at lpdaac.usgs.gov.

2.1.3. MODIS VCF Tree Cover Layer

The MODIS Vegetation Continuous Fields (VCF) Tree Cover version 5 dataset (MOD44B), was produced at 250 m resolution globally from 2000 to 2010 (DiMiceli et al 2011). The MODIS VCF is based on a flexible regression tree algorithm. Although the MODIS Tree Cover VCF has been used for a wide range of continental to global scale assessments, many land cover changes occur in patches smaller than 250 m resolution (Townshend and Justice 1988). Higher resolution continuous field datasets have been generated for limited areas based on Landsat data (e.g., Homer et al. 2004), but there are no global datasets representing tree cover at resolutions finer than that of the MODIS sensor. The MOD44B version 5 dataset can be found on the LP DAAC's Data Pool (https://lpdaac.usgs.gov/tools/data-pool/).

2.2. Algorithm/Theoretical Description

Directional surface reflectance is the most basic remotely sensed surface parameter in the solar reflective wavelengths and therefore provides the primary input for many higher-level surface geophysical parameters, including vegetation indices, albedo, leaf area index (LAI), fraction of absorbed photosynthetically active radiation (FPAR), and burned area. Directional surface reflectance is also used in various applications to visually or quantitatively detect and monitor changes on the Earth's surface.

Nearly half of the original GLS 1990 dataset did not have correct radiometric gain and bias coefficients at the time of data acquisition; thus atmospheric correction and conversion to surface reflectance were not possible (Chander et al. 2003, 2009; Townshend et al. 2012). These un-calibrated GLS images were replaced after the original GLS compilation with substitutes from the updated USGS archive within the epoch wherever possible. To perform the selection of replacement imagery while minimizing phenological or atmospheric noise, a tool was constructed to query the USGS Global Visualization Viewer (GloVis) database (http://glovis.usgs.gov/) for appropriate images based on phenological time series of NDVI from MODIS (Kim et al. 2011; Townshend et al. 2012).

Each image of this enhanced GLS dataset was then atmospherically corrected to surface reflectance using LEDAPS (Masek et al. 2006b). Atmospheric inputs and parameterization of LEDAPS are described by Feng et al. (2013). Clouds were identified in a spectral-temperature space (Huang et al. 2010) and removed from subsequent analysis. This "aggressive" cloud-detection algorithm's low rate of omission error makes it suitable for masking pixels from forest cover change analysis. Cloud shadows were identified by projecting cloud masks onto a digital elevation model through solar geometry at the time of image acquisition (Huang et al. 2010) and were also removed from analysis.

2.2.1. Surface Reflectance Algorithm

2.2.1.1. Radiometric calibration and estimation of top-of-atmosphere reflectance

The Landsat-7 ETM+ instrument has been carefully calibrated and monitored since launch in 1999, and the calibration has been stable since shortly after launch (Markham et al. 2003). The

Landsat-5 calibration history has recently been updated (Chander & Markham 2003, Chander et al. 2009) and is compatible with subsequent Landsat-7 ETM+ data. LEDAPS uses updated calibration histories to convert 8-bit quantized Landsat data to at-sensor radiance and then to top-of-atmosphere (TOA) reflectance using solar geometry and instrument band pass information.

2.2.1.2. Atmospheric correction to estimate surface reflectance

Atmospheric correction seeks to estimate surface reflectance by compensating for the scattering and absorption of radiance by atmospheric constituents. In practice, atmospheric correction is typically achieved by inverting a highly parameterized model of atmospheric radiative transfer coupled to a surface reflectance model. For speed and simplicity, the reflecting surface is often assumed to be Lambertian. In an idealized case of a Lambertian surface (i.e., with angularly uniform reflectance) and in a narrow spectral band (here referred to with the index^{i}) outside of the main absorption feature of water vapor, the top of atmosphere (TOA) signal can be written as (Vermote et al. 1997):

$$\rho^i_{TOA}(\theta_s,\theta_v,\phi,A,\overbrace{\tau^i_A,\omega^i_0,P^i_A}^{Aer^i},U_{H_2O},U_{O_3}) = Tg^i_{OG}(m,A)Tg^i_{O_3}(m,U_{U_{O_3}})\begin{bmatrix}\rho^i_{atm}(\theta_s,\theta_v,\phi,A,Aer^i,U_{H_2O})+ \\ Tr^i_{atm}(\theta_s,\theta_v,A,Aer^i)\dfrac{\rho_s}{1-S^i_{atm}(A,Aer^i)\rho_s}Tg^i_{H_2O}(m,U_{U_{H_2O}})\end{bmatrix}, \quad (1)$$

where:

ρTOA is the top of the atmosphere reflectance;
Tg is the gaseous transmission by a gas species (g), e.g., water vapor (TgH_2O), ozone (TgO_3), or other gases, $TgOG$ (e.g. CO2…);
ρatm is the intrinsic reflectance of the atmosphere;
$Tratm$ is the total atmospheric transmission (downward and upward);
$Satm$ is the spherical albedo of the atmosphere;
A is the atmospheric pressure, which influences the number of molecules and the concentration of absorbing gases in the radiation's path;
τA, $\omega 0$ and PA describe the aerosol properties and are spectrally dependent:
- τa is the aerosol optical thickness;
- $\omega 0$ is the aerosol single scattering albedo;
- PA is the aerosol phase function;

UH_2O is the integrated water vapor content;
UO_3 is the integrated ozone content;
m is the air-mass, computed as $1/\cos(\theta s)+1/\cos(\theta v)$; and
ρS is the surface reflectance to be retrieved.

The geometrical conditions are described by the solar zenith angle (θs), the viewing zenith angle (θv), and by Φ, the difference between θs and θv. The effects of water vapor on the intrinsic atmospheric reflectance is approximated as:

$$\rho^i_{atm}(\theta_s,\theta_v,\phi,A,Aer^i,U_{H_2O}) = \rho^i_R(\theta_s,\theta_v,\phi,A) + \left(\rho^i_{R+Aer}(\theta_s,\theta_v,\phi,A,Aer^i) - \rho^i_R(\theta_s,\theta_v,\phi,A)\right)Tg^i_{H_2O}(m,\frac{U_{U_{H_2O}}}{2}), \quad (2)$$

where ρR represents the reflectance of the atmosphere due to Rayleigh scattering and ρR+Aer represents the reflectance of the mixing molecules and aerosols. Accounting correctly for mixing and coupling effects is important for achieving high accuracy in modeling the atmospheric effect. Eq. (2) conserves the correct computation of the coupling and assumes that the water vapor is mixed with aerosols and that the molecular scattering is not affected by water vapor absorption.

The transmission, intrinsic reflectance, and spherical albedo terms are computed using the vector version of the 6S radiative transfer code (Kotchenova et al. 2006). Since the cost of running 6S for each pixel would be prohibitive, 6S was run early in the process to generate a look up table (LUT) accounting for pressure, water vapor, ozone, and geometrical conditions over the whole scene for a range of aerosol optical thicknesses. The LUT was created for each TM band and was used both in the aerosol retrieval process as well as in the correction step at the end.

Ozone concentrations were derived from Total Ozone Mapping Spectrometer (TOMS) data aboard the Nimbus-7, Meteor-3, and Earth Probe platforms. The gridded TOMS ozone products are available since 1978 at a resolution of 1.25º longitude and 1.00º latitude from the NASA Goddard Space Flight Center Data Active Archive Center (GFSC DAAC). In cases where TOMS data were not available (e.g., 1994–1996), NOAA's Tiros Operational Vertical Sounder (TOVS) ozone data were used. Column water vapor was taken from NOAA National Center for Environmental Prediction (NCEP) reanalysis data available at a resolution of 2.5 by 2.5 degrees (https://rda.ucar.edu/datasets/ds090.0/) over the Landsat era. Digital topography (1 km GTopo30) and NCEP sea-level surface pressure data were used to adjust Rayleigh scattering to local conditions.

Like other atmospheric correction schemes for MODIS and Landsat, the Dark, Dense Vegetation (DDV) method (Kaufman et al. 1997; Remer et al. 2005) was used to infer aerosol optical thickness (AOT) from each image. Based on the correlation between chlorophyll absorption and bound water absorption, this method postulates a linear relation between surface reflectance in the atmospherically insensitive shortwave-infrared (SWIR) (2.2 μm) and surface reflectance in the affected visible bands. The method then uses this relation to calculate surface reflectance for the visible bands and estimate aerosol optical thickness by comparing the result to the TOA reflectance. For LEDAPS AOT estimation, each image was averaged to 1-km resolution to suppress local heterogeneity, and candidate "dark targets" of TOA reflectance were selected. For these targets, correlation was assumed only between the blue (0.45–0.52 μm) and SWIR (2.2 μm) bands, such that water targets were excluded. The specific relation was derived from an analysis of data from Aerosol Robotic Network (AERONET) sites where AOT is measured directly. The calculated AOT in the blue wavelengths was propagated across the spectrum using a continental aerosol model. A "reasonability check" for the aerosol was performed by analyzing the surface reflectance derived in the red band for each 30-m pixel contained in the 1-km grid cell; if too many "unphysical" values were found, the aerosol retrieval at this 1-km location was rejected. The valid AOT at 1 km were interpolated spatially between the dark targets using a spline algorithm. The interpolated AOT, ozone, atmospheric pressure, and water vapor were supplied to the 6S radiative transfer algorithm, which then inverts TOA reflectance to surface reflectance for each 30-m pixel.

As noted above, water targets were excluded from the aerosol retrieval. However, interpolation of valid (i.e., land) aerosol targets occurs across the entire scene. Thus, the surface reflectance of small lakes surrounded by land was likely to be reasonable, while the reflectance of open ocean water (far from any valid aerosol target) was likely to be problematic.

2.2.1.3. Cloud and Shadow Masking

Removing pixels contaminated by clouds and their shadows was necessary to avoid erroneous retrieval of surface reflectance and false detection of forest cover change. LEDAPS implemented two cloud masks – a version of the Landsat Automated Cloud Cover Assessment (ACCA) algorithm (Irish 2000) and a more aggressive mask based on MODIS spectral tests (Ackerman et al. 1998). Shadows were located from the latter using solar geometry and an estimate of cloud height based on the temperature difference between known cloudy pixels and NCEP surface temperature. A third cloud-masking algorithm has been developed by Dr. Vermote through his USGS-funded Landsat Science Team project – "A Surface Reflectance Standard Product for LDCM and Supporting Activities". Quality Assessment codes for this algorithm are listed in Table 1. Finally, an automated cloud and shadow masking algorithm has also been developed by Huang et al. (2010) as part of the TDA-SVM algorithm.

2.2.2. Tree Cover Algorithm

Spatio-temporal estimates of tree-canopy (or simply "tree") cover provide a biophysically relevant, sensible, and consistent basis for monitoring forest cover and change (Sexton et al. 2016). The following algorithm and its results have been peer-reviewed and are described by Sexton et al. (2013b).

2.2.2.1. Model

Tree cover (C) was estimated as a piecewise-linear function of surface reflectance and temperature:

$$C_{i,t} = f(X_{i,t}) + \varepsilon, \qquad (3)$$

where X is a vector of surface reflectance and temperature estimates, ε is error in the estimates produced by *f*() applied to X, subscript *i* denotes the pixel's location in space, indexed by pixel, and *t* refers to its location in time, indexed by year. Continuous measurements such as percent cover and surface reflectance are robust to changes in resolution (Gao et al. 2006, Feng et al. 2013). Although the data were derived from Landsat, the model makes no specification of scale and thus may be calibrated and applied at arbitrary, even different, resolutions between those of Landsat (30 m) and MODIS (250 m). To estimate tree cover at 30 m resolution in 2000 and 2005, MODIS-based, 250 m tree cover estimates were overlaid on rescaled Landsat surface reflectance layers in each year, and a joint sample of cover and reflectance variables was drawn to generate a training dataset for each Landsat scene in each epoch (Figure 5). Throughout this section, data used to estimate model parameters is referred to as "training" data, and data whose accuracy is assumed is referred to as "reference" data.

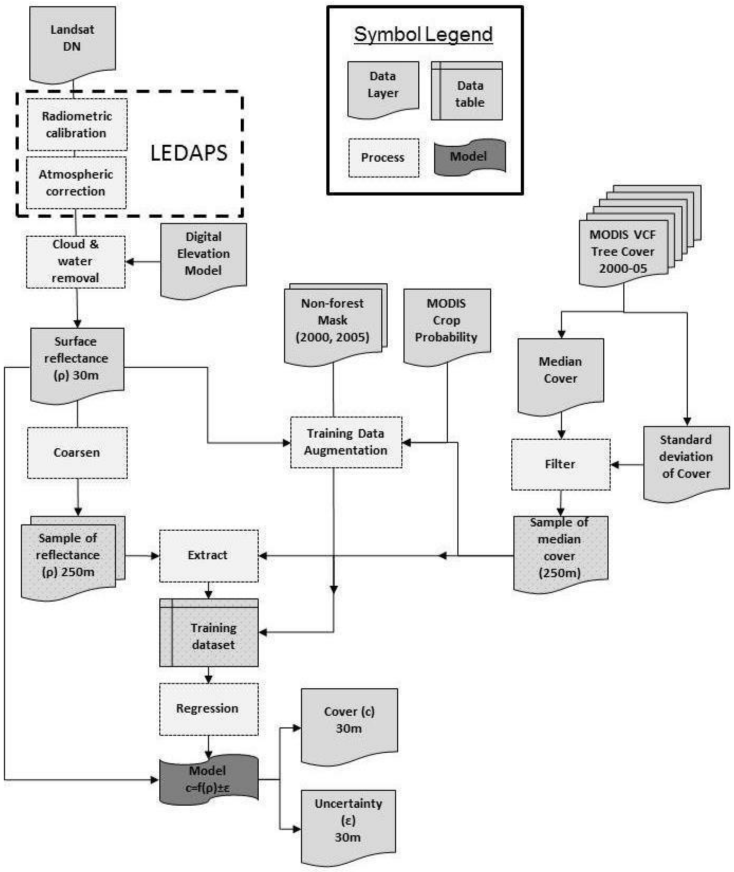

Figure 5. Flowchart of tree cover rescaling algorithm.

The model was thus fit locally to each scene of the Landsat tiling system of WRS-2 in each epoch. The model was fit using the Cubist™ regression tree algorithm and applied using CubistSAM, an open-source parser for Cubist (Quinlan 1993). Except for an allowance for extrapolation within the range [0,100], our application of regression trees was standard. Cubist, as well as regression trees in general, has been found to provide accurate estimates of percent-scale land cover attributes in numerous studies (e.g., Sexton et al. 2006, 2013a). Because regression trees can over-fit the data and there are often few data points at the extremes of the range of the response variable (e.g., tree cover), Cubist gives an option for either estimating within the range of the response variable at each node (default) or extrapolating within a specified range. To avoid over-fitting to the sometimes small samples at terminal nodes with extreme cover values, we allowed for extrapolation within the range of 0-100% tree cover. The fitted model was then applied to the original 30 m Landsat data in order to estimate tree cover at the Landsat spatial resolution.

2.2.2.2. Training Data

"Training" tree-cover data for model fitting were derived primarily from the 250-m MODIS VCF Tree Cover layer (DiMiceli et al. 2011) from 2000-2005. Random errors (i.e., those which were not systematic, e.g., bias) were minimized by using the six-year median of cover for each pixel. Land cover changes between 2000 and 2005 were removed by calculating the standard deviation of annual tree cover estimates for each pixel over that interval and removing pixels in the top 10% of the distribution of standard deviations of each Landsat scene. Because only six years of MODIS VCF data were available, we used the median, which is a better representation of central tendency than the mean in small samples such as the six values of cover from 2000-2005.

Pure (i.e., 0% or 100%) and near-pure pixels are rare in the MODIS data, and tree cover tends to be overestimated in areas of low cover, especially agricultural fields. To ameliorate under-representation of low tree-cover in the training sample, we augmented the MODIS- derived reference data with information from the Training Data Automation and Support Vector Machines (TDA-SVM) automated classification algorithm (Huang et al. 2008) and the MODIS Cropland Probability Layer (Pittman et al. 2010). Cropland Probability and Tree Cover images were overlaid within each Landsat scene, and Landsat pixels with crop probability > 0.5 and tree cover < 50% were selected. This selection comprised Landsat pixels with either crop or sparse vegetation cover. Within the selection, Landsat pixels identified by TDA-SVM as "non-forest" in both 2000 and 2005 were assumed to be sparsely vegetated and were labeled as 0% tree cover. The remaining (i.e., crop) pixels in the selection were ranked by their NDVI values and divided into three sub-strata: high, medium, and low NDVI. Pixels from each of these sub-strata were randomly sampled such that the maximum proportion of Landsat "crop" pixels was the proportion of MODIS pixels within the scene whose crop probability was > 60%. All of the sparsely vegetated pixels and the sample of crop pixels were then pooled with the MODIS-based reference data to form an ensemble training sample of tree cover and reflectance.

2.2.2.3. Post-processing: Water Mask

Surface waterbodies were masked from the tree and forest-cover & change data, and the surface water layer is a useful input to many other applications. The algorithm below (eq. 4) is described by Feng et al. (2015). Water cover was defined as a state of the landcover domain $c \in C$, and its probability of occurrence in each pixel was modeled as a function of reflectance and topographic covariates (X):

$$P(c = \text{"water"}|X) \qquad (4)$$

where *f* is a binary decision tree fit by the See5™ algorithm (Quinlan 1986, 1993). The topographic covariates were elevation and slope derived from the ASTER GDEM (Tachikawa 2011), reflectance covariates were Landsat Band 5 (SWIR) surface reflectance, the Normalized Difference Water index (NDWI) (McFeeters 1996) and the Modified Normalized Difference Water index (MNDWI) (Xu 2006) to distinguish water from other cover types, as well as the NDVI (Tucker et al. 2005) to distinguish water from vegetation specifically. The optimal threshold of each index for separating water varies regionally and over time due to mixing and local similarities with other cover types (Ji et al. 2009; Jiang et al. 2014).

Water was detected in each 30-m Landsat pixel with a classification-tree model (Quinlan 1986) parameterized through an automated, two-stage procedure. An initial, deductive stage identified reference water pixels of varying certainty by comparing multi-spectral water and topographic indices to coarse-resolution (MODIS) water estimates. This stage leveraged prior knowledge with multiple sources of independent information to stratify the decision space into regions of possible water with varying degrees of certainty. An inductive stage then optimizes rules based on high resolution estimates of surface reflectance, brightness temperature, and terrain elevation. The first stage of classification generates local reference data with varying levels of certainty. The pixels, identified as water by multi-spectral indices, were compared with *a priori* water pixels resampled from the 250 m resolution MODIS water mask to the spatial resolution and extent of each Landsat image. This comparison resulted in four possible levels of certainty, through which weights were assigned to each reference datum.

Topographic, spectral, and brightness temperature variables were first stratified into generic cover types: water, land, snow and ice, and cloud. A loose and a strict threshold—equaling - 0.1 and 0.1—were applied each to NDWI and MNDWI to distinguish water with low and high certainty. Terrain shadows were identified as pixels with hill-shade value <150 (on a scale from 0 to 255) and slope >20 degrees. Snow and ice show high reflectance values in the visible and near infrared (NIR) bands and low reflectance in SWIR bands, leading to high MNDWI but low to moderate NDWI. A strict difference threshold (0.7) was used to reduce confusion of water with snow and ice, and a criterion of brightness temperature <1.5 ℃ was also included to further improve the discrimination:

$$\mathrm{MNDWI} > \mathrm{NDWI} + 0.7 \text{ and } \rho_6 < 1.5\ ℃ \,. \tag{8}$$

2.2.3. Forest Cover and Change Algorithm

2.2.3.1. Forest cover and change from 2000-2005

The following algorithm and its results have been peer-reviewed and are described by Sexton et al. (2015).

2.2.3.2. Defining forest Cover

"Forest" is defined as a class of land cover wherein tree (-canopy) cover, *c*, exceeds a predefined threshold value, c^*. The probability of belonging to "forest", $p(F)$, is therefore the probability of *c* exceeding the threshold c^* (Figure 11)—i.e., the integral of the density function of *c* above c^*:

$$p(F) \overset{\text{def}}{=} p(c > c^*) = \int_{c^*}^{100} p(c)dc. \tag{17}$$

Complementarily, the probability of membership in non-forest is simply 1-$p(F)$. In any location *i*, tree cover *ci* is estimated by a model *f* of remotely sensed variables ***X*** (Hansen et al. 2003, Homer et al. 2004, Sexton et al. 2013b):

$$c_i = f(\boldsymbol{X}; \beta) + \varepsilon_i, \tag{18}$$

where β is a set of empirically estimated parameters, and ε is residual error.

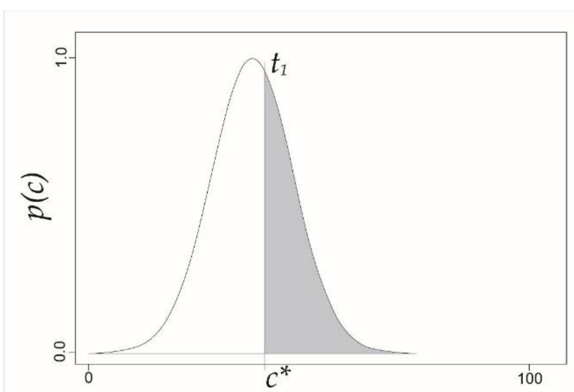

Figure 11. Estimation uncertainty of tree and forest cover within a pixel, modeled as a normal probability density function of tree cover, with probability of forest (shaded) and non-forest (unshaded) defined relative to a threshold of tree cover, c*.

Given a joint sample of locations $i = [1,2,\dots n]$ with coincident true and estimated values of a continuous variable such as tree cover (*ci*, ̃i), error may be quantified as the Root-Mean-Square Error (RMSE), which for large samples approximates the standard deviation of estimates of the true value of cover:

$$\sigma_\varepsilon = \sqrt{\frac{\sum_i (c_i - \hat{c}_i)^2}{n-1}}. \tag{19}$$

Thus, given *ci*, and an estimator (e.g., linear regression) producing estimate ̂and root- mean-square error σi = σ, a Normal probability distribution of possible values of *ci* may be assumed (Snedecor and Cochran 1989, Hastie et al. 2001, Clark 2007):

$$p(c_i) \stackrel{\text{def}}{=} N(\hat{c}_i, \sigma^2) = \frac{1}{\sigma\sqrt{2\pi}} e^{-\frac{(c_i - \hat{c}_i)^2}{2\sigma^2}}. \tag{20}$$

Given paired estimates of cover and its RMSE, this model provides a probability density function of tree cover *p(c)* (Eq. 13) and therefore the probability of identifying forest for each pixel *i* (Eqn. 10).

2.2.3.3. Change Detection Based on Bi-Temporal Class Probabilities

Given the probability of detecting forest in a location *i* = (x,y) at each of two times *t*, four dynamic classes (D) are possible: stable forest (FF), stable non-forest (NN), forest gain (NF), and forest loss (FN). Calculating the probability of each of these dynamics at that location simply requires calculating the following joint probabilities:

$$p(FF)_i = p(F_{i,1}, F_{i,2}) = p(F_{i,1}) \times p(F_{i,2}) \tag{21}$$

$$p(NN)_i = p(N_{i,1}, N_{i,2}) = \left(1 - p(F_{i,1})\right) \times \left(1 - p(F_{i,2})\right) \tag{22}$$

$$p(NF)_i = p(N_{i,1}, F_{i,2}) = \left(1 - p(F_{i,1})\right) \times p(F_{i,2}) \tag{23}$$

$$p(FN)_i = p(F_{i,1}, N_{i,2}) = p(F_{i,1}) \times \left(1 - p(F_{i,2})\right) \tag{24}$$

where subscripts denote observation times (Figure 12). In practice, the model of error is approximate, and so carets (^) denote that the resulting values are estimates. These joint probabilities sum to unity at each location *i*, and because they are merely transformations of the original cover and error values in every pixel, they may be mapped geographically without gain or loss of information from those estimates. In order to produce a categorical map of change classes, each pixel may be assigned either the most probable class at *i*, or some other criterion of probability may be set (e.g., $p \geq 0.9$) to filter detection based on certainty of the tree-cover and derived forest-cover and -change estimates.

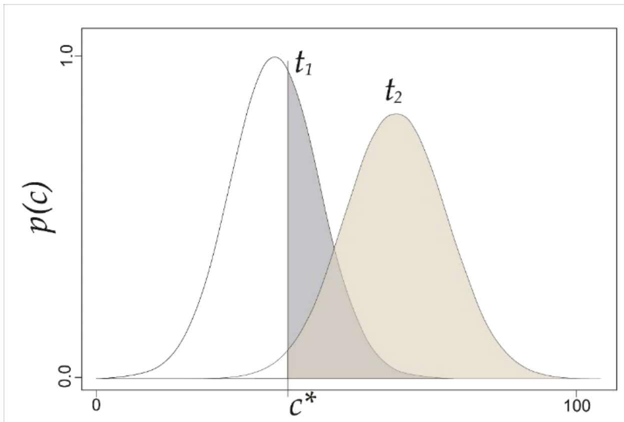

Figure 12. Categorical (forest) change detection based on probabilistic fields of tree cover at two times, t_1 and t_2.

2.2.3.4. Forest Cover and Change from 1990-2000

The following algorithm and its results have been peer-reviewed and are described by Kim et al. (2014).

2.2.3.5. Forest Cover Retrieval

We inferred forest cover in 1990 and change from 1990 to 2000 using a signature-extension approach based on stable pixels hind cast from 2000 and 2005 epochs (Figure 13). For the purpose of large-area mapping, extrapolation of models beyond the immediate temporal and spatial domain in which they were trained has been explored by many researchers (Sexton et al. 2013b; Gray and Song 2013). Termed as "generalization" or "signature extension", this approach has been successfully applied for the classification of forest cover (Pax-Lenney et al. 2001) and change (Woodcock et al. 2001) using Landsat data. This approach also has been implemented by deriving training data from one date and using it to train a classifier on a different image from the same path/row scene but different acquisition date (Pax-Lenney et al. 2001). Complementary to the traditional signature extension method, Gray and Song (2013) combined a procedure to identify stable pixels to deal with irregular time series images.

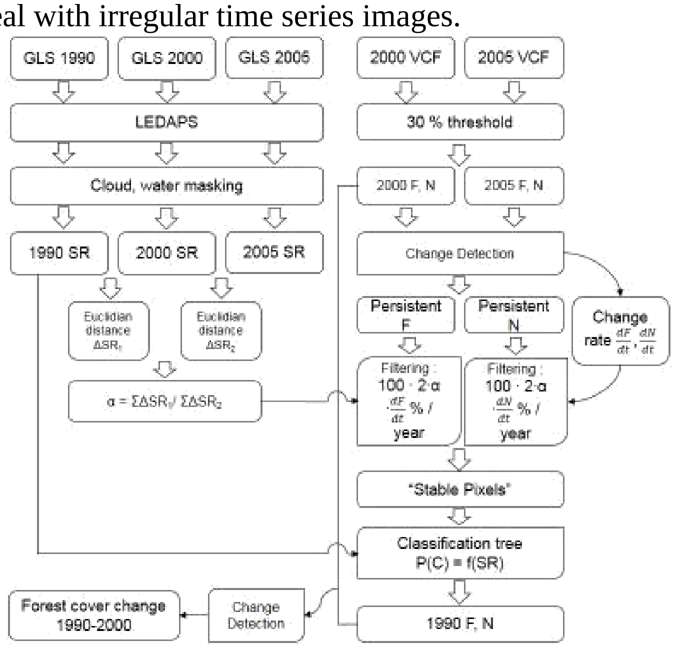

Figure 13. Hind-cast training and classification procedure to retrieve historical forest cover estimates. SR = surface reflectance, C = cover, t1 ≈ 1990, and tn≈ 2000 or 20005.

2.2.3.6. Reference Forest/Non-Forest Data

Persistent forest (F) and non-forest pixels (N) were sampled from forest cover change maps between the 2000 and 2005 GLS epochs and then filtered so that only "stable" pixels—i.e., those whose class did not change between the 1990 and 2000 epochs—were retained for analysis. The details of the filtering process are presented below.

For each WRS-2 scene, an annual rate of forest-cover (F) change, $\frac{dF}{dt}$, and an annual rate of non-forest cover (N) change, $\frac{dN}{dt}$, were calculated as:

$$\frac{dF}{dt} = \frac{|F_{t2} - F_{t1}|}{t2-t1} \tag{25}$$

$$\frac{dN}{dt} = \frac{|N_{t2} - N_{t1}|}{t2-t1} \tag{26}$$

where F and N are the percentage of forest and non-forest pixels, respectively, and t_1 and t_2 are respectively the acquisition years of the Landsat images for the 2000 and 2005 GLS epochs.

The spectral difference (ΔSR) - quantified as the Euclidean distance between two pixels over time in the spectral domain–was calculated for 1990-2000 (ΔSR_1) and 2000-2005 (ΔSR_2). To minimize impact from accelerating or decelerating rates of forest cover change between two periods, a parameter α was defined as the ratio of the sums of spectral difference of all persistent pixels and was calculated as:

$$\alpha = \Sigma\Delta SR_1 / \Sigma\Delta SR_2, \tag{27}$$

Given the large number of available pixels within the overlapping portion of two Landsat images within the same WRS-2 scene, α was doubled to increase the selectivity of filtering for stable pixels. A percentage of forest equaling α x 2 x 100 × $\frac{dF}{dt}$, and non-forest pixels equaling α x 2 x 100 × $\frac{dN}{dt}$ were thus removed per year of difference between 1990- and 2000-epoch images in the order of spectral difference (ΔSR). Limiting the sample to pixels that were stable from 2000 to 2005 minimized inclusion of erroneous data, and filtering the most spectrally different pixels from 1990 to the later epochs removed the pixels most likely to have changed over that period.

2.2.3.7. Forest Cover Classification

Using the sample of stable-pixel locations, a forest/non-forest reference sample was extracted from forest cover maps in 2000 and 2005. This sample was then filtered to maximize certainty and minimize change between observation periods (Figure 13).

Forest cover in circa-1990 was retrieved by a classification-tree algorithm. The probability of forest cover, p(F), in each pixel i at time $t \approx 1990$ was estimated by a conditional relationship (g) to remotely sensed covariates (X):

$$\hat{p}(F)_{i,t} = g(X_{i,t}), \tag{28}$$

where X is a vector of surface reflectance and temperature estimates; subscripts i and t denote the pixel's location in space, indexed by pixel, and time indexed by year. The relation g was parameterized using the C 5.0 ™ classification-tree software (Quinlan 1986), trained on a sample of pixels within each Landsat image; the model was thus fit locally within each Landsat WRS-2 scene. Reflectance and temperature covariates were acquired from the GLS 1990 (Gutman et al. 2008) and other Landsat images selected from the USGS archive. Whereas retrievals from within the period of overlap between the Landsat-5, Landsat-7, and MODIS eras may be based on general—even global—models based on phenological metrics that require dense image samples within each year (e.g., Hansen et al. 2013), this local fitting instead maximizes use of the single-image coverage characteristic of much of the history of the Earth observation. Use of atmospherically corrected surface reflectance fulfills the conditions for signature extension in space (Woodcock et al. 2001, Pax-Lenney et al. 2001).

Decision trees and other empirical classifiers are sensitive to bias in training samples relative to class proportions within their population of inference (Borak 1999, Carpenter et al. 1999, Woodcock et al. 2001, Sexton et al. 2013c) and to uncertainty in the training data set (McIver 2002, Strahler 1980). To minimize these effects, we maintained a large sample with representative class proportions by removing a small, but equal fraction of the least stable pixels from each class while maintaining the class proportions from reference epoch to training sample. Further, we weighted each pixel's contribution to the classifier's parameterization based on the pixel's classification certainty in the reference data. A weight *w* was adopted for each pixel as the classification probability of the estimate (*pmax*) of forest-or non-forest cover (C) from the 2000-epoch dataset:

$$W_i = p_{max}(C_i). \tag{29}$$

The weights were then applied to adjust the objective (i.e., purity) function maximized by the iterative binary recursion algorithm employed by C5.0™ (Quinlan 1986).

2.2.3.8. Forest-cover change

Classification trees estimate the probability *p(C)* of each class in each pixel as a conditional relative frequency. Given C = "F" (i.e., "forest"), each pixel was labeled either "forest" or "non-forest" based on *p(F)*:

$$F \stackrel{\text{def}}{=} p(F) \geq 0.5 \tag{30}$$

$$N \stackrel{\text{def}}{=} p(F) < 0.5 \tag{31}$$

Forest cover change between the 1990 and 2000 epochs was detected given the joint probabilities in the 1990 and 2000 epochs (Sexton et al. 2015):

$$p(FF_i) = p(F_{it_1}) \times p(F_{it_2}) \tag{32}$$

$$p(NN_i) = \left(1 - p(F_{it_1})\right) \times \left(1 - p(F_{it_2})\right) \tag{33}$$

$$p(NF_i) = \left(1 - p(F_{it_1})\right) \times p(F_{it_2}) \tag{34}$$

$$p(FN_i) = p(F_{it_1}) \times \left(1 - p(F_{it_2})\right) \tag{35}$$

That is, given the probability of forest P(F) vs. non-forest P(N) in a pixel *i* in the 1990 epoch (t_1) and 2000 epoch (t_2), four classes were derived: stable forest (FF), stable non-forest (NN), forest gain (NF), and forest loss (FN). A categorical map of change classes was then produced by assigning each pixel the class with the highest probability.

2.2.3.9. Post-processing

2.2.3.9.1. Hedge rule

In the forest cover change products, the forest dynamics (i.e., forest loss and forest gain) between two periods were determined by checking the joint probabilities of forest and non-forest estimated for each of the dates (Kim et al. 2014; Sexton et al. 2015). Dynamic classes are more difficult to detect than stable classes, and a criterion is applied to filter the detected change estimates (Kim et al. 2014; Sexton et al. 2015). According to the investigation, commission and omission errors reached the closest point when the criterion is near 0.6 for both forest loss and forest gain. The threshold 0.6 was, therefore, applied to the production of the forest cover change datasets to produce unbalanced estimations of the global forest dynamics.

2.2.3.9.2. Minimum Mapping Unit

A minimum mapping unit (MMU) was applied to comply with the forest definition and also to minimize erroneous detection of change due to spatial misregistration of Landsat images. Raster polygons smaller than the threshold MMU (0.27 hectare, or 3 pixels) were replaced by the class of the largest neighboring polygon. An eight-neighbor rule was used to delineate patches, which includes diagonally connected neighbors.

3. Data Products

3.1. Dataset Characteristics/Collection Details

The GFCC collection contains multiple products, each containing different characteristics. Table 1 below summarizes the attributes of each available data product.

Table 1. Dataset characteristics for each product in the GFCC collection.

Dataset	**FR-SR ESDR**	**FR-FCC ESDR**	**FR-WM**	**Tree Cover Product**
Description	Fine resolution surface reflectance earth science data record	Fine resolution forest cover and change earth science data record	Fine resolution water mask that was used in making the FCC product	Tree cover ancillary product
Spatial Resolution	30 m	30 m	30 m	30 m
Temporal Resolution	NA	NA	NA	NA
Spatial Coverage	Global	Global	Global	Global
Temporal Coverage	1990, 2000, 2005, 2010	1990-2000, 2000-2005	2000	2000, 2005, 2010, 2015
Format	GeoTIFF	GeoTIFF	GeoTIFF	GeoTIFF
Data Type	16 bit signed integer	CM: 8 bit unsigned integer CP: 32 bit floating point	8 bit unsigned integer	8 bit unsigned integer
Projection	UTM	UTM	UTM	UTM
Datum	WGS-84	WGS-84	WGS-84	WGS-84

3.1.1. Fine Resolution Surface Reflectance Earth Science Data Record Product

The fine resolution surface reflectance earth science data record (FR-SR ESDR) product contains global 30 m resolution estimates of surface reflectance for four epochs centered on the years 1990, 2000, 2005, and 2010. The data are derived from the Global Land Survey (GLS). The FR-SR ESDR product was tiled using the WRS-2 tiling scheme.

3.1.1.1. FR-SR ESDR Product Contents

The FR-SR ESDR product is distributed in compressed GeoTIFF files, and contains the science datasets (SDs) shown in Table 2. Each surface reflectance folder has 13 files associated with it; a surface reflectance file for each band, an Atmospheric Opacity file and the Landsat SR Quality file. See the example below:

- **p001r012_7dt20110812.SR.b01-b07.tif:** files that contains a GeoTIFFs of the SR product for bands 1 – 7.
- **p001r012_7dx20110812.SR.AO.tif:** file that contains a single GeoTIFF of the atmospheric opacity of band 1.
- **p001r012_7dx20110812.SR.QA.tif:** file that contains a single GeoTIFF of the Landsat SR Quality layer.

Table 2. Description of layers contained in the FR-SR ESDR product.

Science Dataset	Description	Units	Data Type	Fill Value	Valid Range	Scale Factor
SR.b01	Band 1 surface reflectance	Reflectance	16 bit signed integer	-9999	-2000, 16000	0.0001
SR.b02	Band 2 surface reflectance	Reflectance	16 bit signed integer	-9999	-2000, 16000	0.0001
SR.b03	Band 3 surface reflectance	Reflectance	16 bit signed integer	-9999	-2000, 16000	0.0001
SR.b04	Band 4 surface reflectance	Reflectance	16 bit signed integer	-9999	-2000, 16000	0.0001
SR.b05	Band 5 surface reflectance	Reflectance	16 bit signed integer	-9999	-2000, 16000	0.0001
SR.b07	Band 7 surface reflectance	Reflectance	16 bit signed integer	-9999	-2000, 16000	0.0001
SR.b06	Band 6 TOA Temperature	Celsius	16 bit signed integer	-9999	-7000, 7000	0.01
SR.AO	Atmospheric Opacity of Band 1	None	16 bit signed integer	-9999	-2000, 16000	0.0001
SR.QA	Landsat SR Quality Layer	None	16 bit signed integer	-1	0, 32767	NA

Table 3: Bit description for the Landsat SR QA file contained in the FR-SR ESDR product.

Quality Flags	Description
Bit 0	Unused
Bit 1	Data Quality flag (0 = Valid data, 1 = Invalid data)
Bit 2	Cloud mask (0 = clear, 1 = cloudy)
Bit 3	Cloud shadow mask
Bit 4	Snow mask
Bit 5	Land mask (0=water, 1=land)
Bit 6-15	Unused

3.1.1.2. FR-SR Naming Convention

p001r012_7dt20110812.SR.: The surface reflectance data products are named using the following convention: ***p*** stands for "path", followed by ***three digits*** which represent the WRS-2 path, then ***r*** which stands for "row" followed by the ***three digits*** which represent the WRS-2 row. Following the underscore there is a number followed by two letters (***7dt***) which is followed by ***eight digits*** which represent the time of acquisition (YYYYMMDD) for the input Landsat data for which the dataset was generated. Finally, each name contains ***.SR.*** which defines the FR-SR product.

3.1.2. Fine Resolution Forest Cover and Change Earth Science Data Record Product

Results of the world's first global forest cover and change product (version 0) were presented at the NASA LCLUC meeting in 2012 and were subsequently published (Townshend et al. 2012). The beta release of the forest cover and change was made available in May 2013 to a select user group to assess the data and get feedback. The product was improved using the feedback and version 1 of the product was released in May 2014.

3.1.2.1. FR-FCC ESDR Product Contents

The fine resolution forest cover and change earth science data record (FR-FCC ESDR) product contains global 30 m resolution estimates of forest cover change from 1990 to 2000 and from 2000 to 2005, and includes per-pixel level accuracy indicators. The derived forest cover product was tiled using the WRS-2 tiling scheme and kept the native resolution information from the tree cover product that was used to generate the forest cover and change product. Each forest cover folder has four files associated with it; a browse file, a preview file, the change map file and the change probability file. See the example below:

- **p015r033_FCC_19902000_CM.tif:** file that contains a single GeoTIFF of the forest cover and change map product.
- **p015r033_FCC_19902000_CP.tif:** file that contains a single GeoTIFF of the forest cover and change probability product.

Table 16: Code values stored in the forest cover and change map product.

Value	Label
0	No Data
2	Shadow
3	Cloud
4	Water
11	Persistent Forest
19	Forest Loss
91	Forest Gain

99	Persistent Non-forest

3.1.2.2. FR-FCC Naming Convention

p015r033_FCC_19902000: The forest cover and change data products are named using the following convention: ***p*** stands for "path", followed by ***three digits*** which represent the WRS-2 path, then ***r*** which stands for "row" followed by the ***three digits*** which represent the WRS-2 row. Between the underscores are three letters (***FCC***) which is the short name for the forest cover and change product, followed by ***eight digits*** which represent the years for which the dataset was generated.

3.1.3. Fine Resolution Water Cover Product

The fine resolution water cover (FR-WC) product contains global 30 m resolution estimates of water from circa-2000. The water cover product is tiled using the WRS-2 tiling scheme.

3.1.3.1. Water Cover Naming Convention

p015r033_WC_20011005: The water cover data product is named using the following convention: ***p*** stands for "path", followed by ***three digits*** which represent the WRS-2 path, then ***r*** which stands for "row" followed by the ***three digits*** which represent the WRS-2 row. Between the underscores are two letters (***WC***) which is the short name for the water cover product, followed by ***eight digits*** which represent the date (***YYYYMMDD)*** of the Landsat data used to derive the water cover mask.

3.1.4. Tree Cover Product

The tree cover data product, though initially an ancillary layer for generating the forest cover and change product, quickly became an important source of information for the user community. The team started generating the product in late 2012 and distributing the data in early 2013. We have processed the GLS 2000, 2005, and 2010 tree cover products. Since there is no MODIS tree cover product for the 1990s, there is no tree cover product before the year 2000. Further improvement of the tree cover product is ongoing with funding support from NASA Carbon Cycle Science and Land Use Land Cover Change programs.

3.1.4.1. Tree Cover Product Contents

The derived tree cover product was tiled using the WRS-2 tiling scheme and kept the native projection information from the Landsat tile. Each tree cover data folder has six files associated with it; data file, a per pixel uncertainty layer, an index file, and a text file. See the example below:

- **p015r033_TC_2000.tif:** file that contains a single GeoTIFF of the tree cover product.
- **p015r033_TC_2000_err.tif:** file that contains a single GeoTIFF of the uncertainty layer for the tree cover product, which provides per pixel uncertainty by WRS-2 tile.
- **p015r033_TC_2000_idx.tif:** The data provenance layer which uses numerical values associated in the *_idx.txt file to allow the user to understand how many and which file each pixel was obtained from to create this single WRS-2 tile.
- **p015r033_TC_2000_idx.txt:** The list of input files that were used to generate each WRS-2 tile.

Table 15: Code values stored in the tree cover data product.

Value	Label
0-100	Percent of pixel area covered by tree cover
200	Water
210	Cloud
211	Shadow
220	Fill Value

3.1.4.2. Tree Cover Product Naming Convention

p015r033_TC_2000: The tree cover data product is named using the following convention: ***p*** stands for "path", followed by ***three digits*** which represent the WRS-2 path, then ***r*** which stands for "row" followed by the ***three digits*** which represent the WRS-2 row. Between the underscores are two letters (***TC***) which is the short name for the tree cover product, followed by ***four digits*** which represent the year (***YYYY)*** for which the dataset was generated.

4. Data Access

All of the NASA GFCC datasets have been made available via the Global Land Cover Facility (GLCF) (www.landcover.org), via the GLCF Earth Science Data Interface (ESDI) and File Transmission Protocol (FTP). Developed with support from the NASA REaSON program, ESDI is a web-based tool for users to search and download data from GLCF's archive using spatial and non-spatial queries. FTP is used by those who are more familiar with the structure of the GLCF archive, those who want to automate data downloading using scripts, and for those who use GLCF as a read-only "cloud" storage solution. ESDI's mapping interface uses Java Server Pages (JSP) coupled with MapServer. JSP handles the user clicks for selecting data and selecting the type of query and passes the attributes to MapServer for displaying the data coverage on the map (Figure 23). This is helpful for users to know if their area of interest has data coverage.

Though the data was initially distributed at GLCF, the data will ultimately be housed at the LP DAAC. As of now all of the data generated from this project have been transferred to the LP DAAC for archive and can be found at lpdaac.usgs.gov.

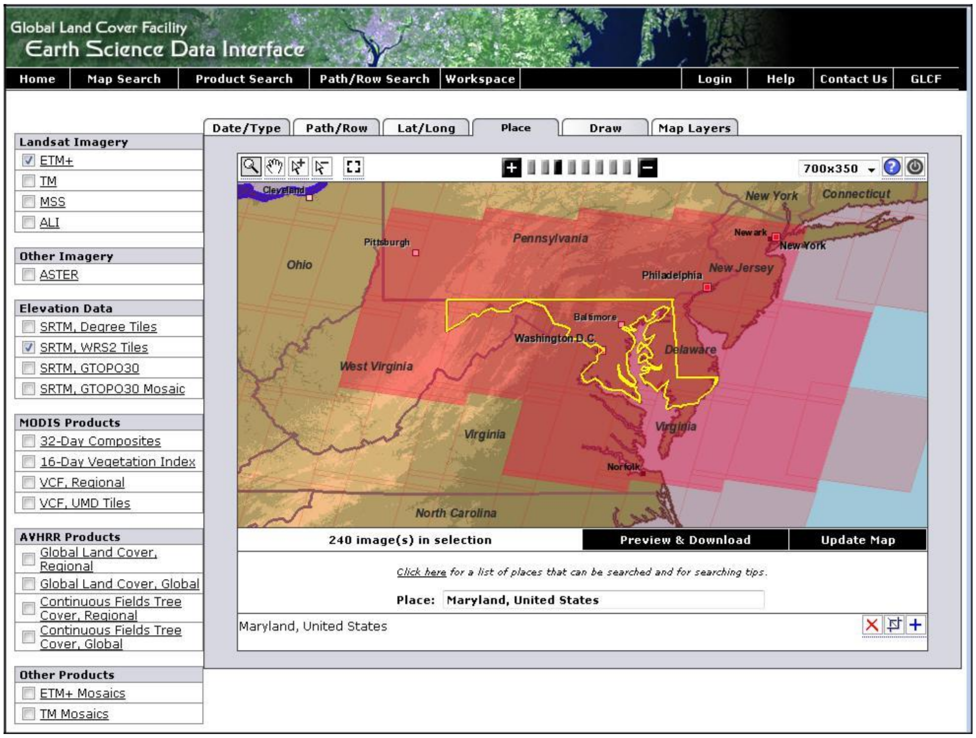

Figure 23. A user has selected Landsat ETM+ and SRTM dataset for the state of Maryland. The area highlighted in darker red is the Landsat based WRS-2 tiles that intersect the Maryland state boundary.

5. Validation/Uncertainty

5.1. Validation: Surface Reflectance

Landsat surface reflectance products were validated in two ways. Internal AOT estimates retrieved by LEDAPS have been compared to measurements taken at AERONET observations (Masek et al. 2006b), and surface reflectance was compared to simultaneously acquired MODIS daily reflectance and Nadir BRDF-Adjusted Reflectance (NBAR) images (MOD09 and MOD43, respectively) (Feng et al 2013). These paired validations provide an internal check on a driving parameter of the LEDAPS algorithm (AOT), as well as a consistency check against the thoroughly calibrated and validated MODIS products.

5.1.1. Comparison of Retrieved AOT to AERONET Measurements

Aerosol optical thickness estimates from pixels processed through LEDAPS were compared to coincident measurements from 21 of AERONET sites (Table 2). All AOT values reported are for the blue wavelengths. Results suggest reasonable agreement with AERONET observations, and the discrepancies between LEDAPS and MODIS reflectance products were generally within the uncertainty of the MODIS products themselves—the greater of 0.5% absolute reflectance or 5% of the retrieved reflectance value.

Table 2. AERONET and ETM+ AOT comparisons.

AERONET Site	TM Scene	Date	AOT blue Aeronet	AOT blue ETM+
Howland	p011r029	2002253	0.4	0.1767
GSFC	p015r033	2001278	0.25	0.257
MD_Science_Center	p015r033	2001278	0.29	0.414

SERC	p015r033	2001278	0.25	0.294
BSRN_BAO_Boulder	p033r032	2000261	0.05	0.024
Sevilleta	p034r036	2000130	0.12	0.135
Bratts_Lake	p035r025	2000208	0.2	0.161
Bratts_Lake	p036r025	2001217	0.08	0.026
Maricopa	p036r037	2000167	0.09	0.1889
Tucson	p036r037	2000167	0.11	0.056
UCLA	p041r036	2000122	0.2	0.275
Shirahama	p109r037	2001105	0.3	0.344
Anmyon	p116r035	2001266	0.11	0.156
Moscow_MSU_MO	p179r021	2002150	0.17	0.059
Rome_Tor_Vergata	p191r031	2001215	0.49	0.384
Ilorin	p191r054	2000037	1.05	0.921
Ouagadougou	p195r051	2001195	0.275	0.346
Lille	p199r025	2000237	0.29	0.38
Palaiseau	p199r026	2000237	0.22	0.156
Thompson	p033r021	2001260	0.06	0.033
HJAndrews	p045r029	1999275	0.08	0.033

5.1.1.1. Operational Quality Assessment

A second validation was based on MODIS surface reflectance estimates. With bands corresponding to each of Landsat 7’s solar-reflective bands (Table 3), the MODIS sensor aboard the Terra platform follows the same orbit and crosses the equator roughly 30 minutes behind Landsat-7 ETM+. MODIS surface reflectance data products (MOD09) have been calibrated and validated comprehensively (Vermote et al. 2002, Kotchenova et al. 2006, Vermote and Kotchenova 2008) and may be used as a reference to validate Landsat surface reflectance products (Feng et al. 2012). We developed an online tool for validating Landsat surface reflectance (SR) estimates against coincident MODIS estimates and used it to validate the 2000 and 2005 epoch SR products. Initial tests for WRS-2 scenes over eastern Africa showed strong agreement between Landsat-7 ETM+ and MODIS SR products, with the majority of R^2 value above 0.9.

Table 3. Landsat-7 ETM+ spectral bands and their MODIS counterparts.

Landsat ETM+ Band	ETM+ Bandwidth (nm)	MODIS Band	MODIS Bandwidth (nm)
1	450-520	3	459-479
2	530-610	4	545-565
3	630-690	1	620-670

4	780-900	2	841-876
5	1550-1750	6	1628-1652
7	2090-2350	7	2105-2155

The uncertainty of the tree cover estimate in every pixel was assessed relative to the training data by ten-fold cross-validation. Pixel-level uncertainty was quantified at each terminal node of the regression tree and assigned to pixels identified with that node. Because these pixel-level uncertainties were assessed only relative to their training data, errors between the reference data and actual cover were not included at the pixel level. As described in a later section, training (MODIS) and output estimates were compared to approximately coincident measurements derived from small-footprint lidar measurements in order to assess their accuracy relative to more direct measurements of actual cover. We use the term "measurement" to refer to lidar derived values of cover – which are calculated without statistical inference – and the more general "estimate" to refer to values derived statistically from MODIS and Landsat images. All comparisons were made at 250 m resolution, using MODIS estimates from 2005 and Landsat estimates from the 2005 epoch. Preliminary analyses comparing Landsat estimates to lidar measurements at 30 m resolution were not appreciably different than those reported here, although there was a small reduction of correlation believed to be due to spatial misregistration of Landsat data.

Uncertainty metrics were based on average differences between paired model and reference (or training) values (Willmott, 1982), quantified by Mean Bias Error (MBE), Mean Absolute Error (MAE), and RMSE:

$$\mathrm{MBE} = \sum_{i=1}^{n} \frac{M_i - R_i}{n} \tag{10}$$

$$MAE = \sum_{i=1}^{n} \frac{|M_i - R_i|}{n} \tag{11}$$

$$\mathrm{RMSE} = \sqrt{\frac{\sum_{i=1}^{n} (M_i - R_i)^2}{n}} \tag{12}$$

where M_i and R_i are estimated and reference tree cover values at a location *i* in a sample of size *n*. After modeling the relationship between M and R by linear regression, the (squared) difference was disaggregated into systematic error (*MSES*) and unsystematic error (*MSEU*) based on the modeled linear relationship (Willmott 1982):

$$MSE_S = \sum_{i=1}^{n} \frac{(\widehat{M_i} - R_i)^2}{n} \quad (13)$$

$$MSE_U = \sum_{i=1}^{n} \frac{(M_i - \widehat{M_i})^2}{n} \quad (14)$$

Where $\widehat{M_i}$ is the cover value predicted by the modeled relationship (Willmott 1982). Accuracy is thus quantified by the difference between the trend of model over reference cover, and precision is quantified by the variation surrounding that trend. MSES and MSEU sum to Mean-Squared Error (MSE), and therefore:

$$RMSE = \sqrt{MSE_s + MSE_u} \quad (15)$$

(Willmott 1982). To maintain consistency, we report the square roots of MSES and MSEU, i.e., RMSES and RMSEU, in units of percent cover.

5.1.1.2. Reference Data

For comparison to the 2005 epoch estimates, small-footprint, discrete-return lidar measurements were collected at four sites in a range of biomes (Figure 6): (1) La Selva Biological Station and its vicinity, Costa Rica (CR) in 2006; (2) the Wasatch Front in central Utah (UT), USA in 2008; (3) the Sierra National Forest in northern California (CA), USA in 2008; and (4) the Chequamegon-Nicolet National Forest, Wisconsin (WI), USA in 2005.

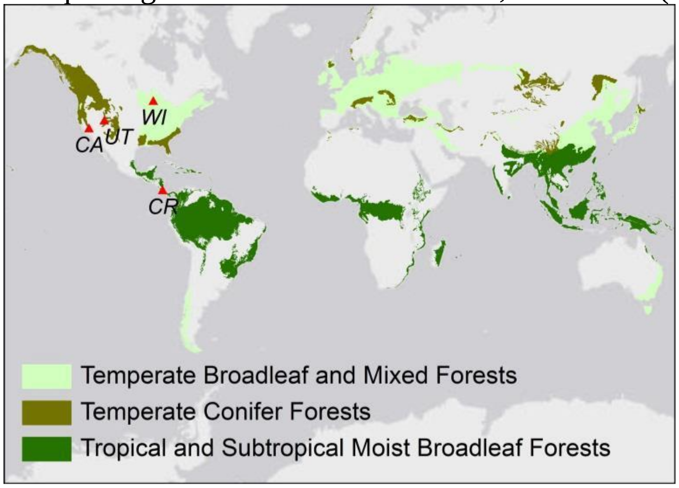

Figure 6. Distribution of lidar-based reference sites, overlaid on global biomes (W 2001). Only the major habitat types intersecting reference sites are shown.

All lidar measurements were acquired during the growing season of each respective site, with mean point densities > 1 return/m^2. The Costa Rica dataset, collected in 2006, is described by Kellner et al. (2009), and the Wisconsin dataset is described by Cook et al. (2009). Figure 7 shows an example of the 3-dimensional distribution of lidar measurements in the California site. All sites were assessed visually for obvious changes in cover between data acquisitions; in the WI dataset, obvious cover changes due to forest harvesting between Landsat and lidar acquisitions (totaling 21 pixels) were delineated manually and removed.

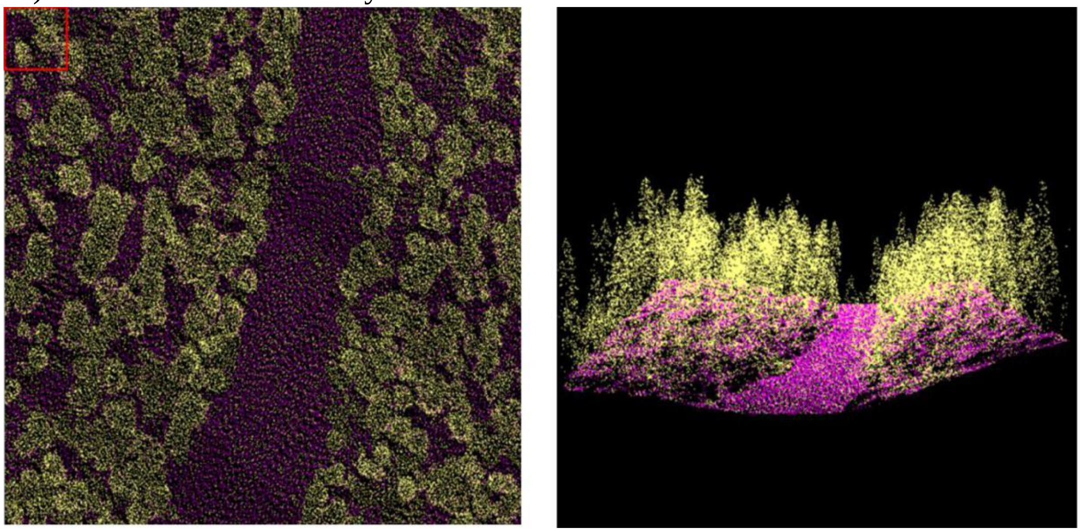

Figure 7. Three-dimensional distribution of a 250x250-m subset of the lidar measurements from the California reference site in nadir (left) and oblique (right) perspectives. Data points, which were sampled with intensity of approximately 13 points/m^2, are classified by height into tree (yellow) and non-tree (pink) classes. The red box in the upper-right corner shows the area of one 30-m Landsat pixel.

Tree cover (C) was calculated from lidar returns by dividing the number of returns above a criterion height by the total number of returns within a 10-m radius:

$$C = \frac{n_h}{n} \tag{16}$$

where n is the number of returns and n_h is the number of returns above the specified height (h) (Korhonen et al. 2011). In accordance with the International Geosphere-Biosphere definition of forests, we specified the criterion n_h = 5 meters. Following calculation of tree cover at 10 m resolution, rasters were aggregated to 250 m resolution by averaging the values within the extent of each 250 m pixel. Only height of the (discrete-return) lidar posts was used to calculate canopy height.

5.1.1.3. Consistency of Landsat- and MODIS-based (VCF) tree cover estimates

The relationship between Landsat estimates of tree cover and the MODIS data on which they were based was very strongly linear, near parity, and consistent among biomes. Relative to the MODIS estimates, Landsat estimates exhibited MBE of -6%, MAE of 8%, and RMSE of 10% cover in the biome samples of 2005 data. The modeled linear relationship explained 88% of the variation between the two datasets, and RMSE was equally partitioned between systematic and random components, with both RMSES and RMSEU equaling approximately 7% cover (Table 7). Although significantly different from zero, the intercept of the linear relationship was relatively small (4.5%). The global Landsat-MODIS VCF comparison for 2000 and 2005 epochs corroborated the aggregated site-specific results, with little difference between epochs. Paired Landsat- and MODIS-based estimates were distributed predominantly along the 1:1 line, with a slight under-estimation of Landsat- relative to MODIS-derived values of cover. Errors were slightly greater in the 2005 than in the 2000 data (RMSE = 8.9% in 2000; RMSE = 11.9% in 2005), and the greatest differences were confined largely to the humid tropics, suggesting their origin might lie in the effects of remnant clouds in the Landsat images.

Table 7. Linear regression summaries for pixel-level canopy cover estimates in four study areas. RMSEu is mean "unsystematic", or "residual" error between original and calibrated measurements, and RMSEs is the "systematic" error remaining between calibrated and reference measurements (see text for full explanation). Unless otherwise noted, all coefficients are significant at Pr(>|t|) < 0.01.

All Sites

Regression	*Intercept (S.E.)*	*Slope (S.E.)*	R^2	*RMSEs*	*RMSEu*
MODIS ~ lidar	12.429 (0.549)	0.714 (0.008)	0.705	10.097	13.462
Landsat ~ MODIS	4.530 (0.323)	0.825 (0.005)	0.882	7.063	7.473
Landsat ~ lidar	10.016 (0.384)	0.668 (0.006)	0.811	14.637	9.406

Costa Rica (n=2044)

Regression	*Intercept (S.E.)*	*Slope (S.E.)*	R^2	*RMSEs*	*RMSEu*
MODIS ~ lidar	29.621 (0.756)	0.561 (0.010)	0.628	11.242	10.573
Landsat ~ MODIS	12.477 (0.572)	0.710 (0.008)	0.804	9.765	6.066
Landsat ~ lidar	24.593 (0.380)	0.517 (0.004)	0.850	16.640	5.312

California (n=289)

Regression	*Intercept (S.E.)*	*Slope (S.E.)*	R^2	*RMSEs*	*RMSEu*
MODIS ~ lidar	23.963 (1.835)	0.517 (0.042)	0.348	6.610	8.226
Landsat ~ MODIS	16.031 (1.548)	0.603 (0.033)	0.539	4.583	5.687
Landsat ~ lidar	22.248 (1.328)	0.506 (0.030)	0.494	5.893	5.955

Utah (n=425)

Regression	*Intercept (S.E.)*	*Slope (S.E.)*	R^2	*RMSEs*	*RMSEu*
MODIS ~ lidar	6.069 (0.453)	0.365 (0.016)	0.552	13.556	5.500
Landsat ~ MODIS	-1.066 (0.372)	0.807 (0.022)	0.755	4.160	3.784
Landsat ~ lidar	3.316 (0.453)	0.318 (0.016)	0.483	16.766	5.492

Wisconsin (n=655)

Regression	*Intercept (S.E.)*	*Slope (S.E.)*	R^2	*RMSEs*	*RMSEu*
MODIS ~ lidar	22.759 (0.888)	0.390 (0.013)	0.561	21.456	8.708
Landsat ~ MODIS	3.128 (1.384)*	0.941 (0.028)	0.619	0.856	9.699
Landsat ~ lidar	17.119 (0.809)	0.508 (0.012)	0.728	18.185	7.849

5.1.1.4. Accuracy of Landsat-based Tree Cover Estimates Relative to Lidar Reference Data

Across the four sampled biomes, the correspondence of Landsat-based estimates of tree cover to reference lidar measurements was similar to the relationship between MODIS-based estimates and lidar-based measurements. Across the biomes, RMSE of Landsat estimates relative to lidar-measured cover was 17%, with MAE of 15% and MBE of -11% cover. However, the overall linear relationship between Landsat estimates and lidar measurements was stronger (R^2 = 0.81) than that of MODIS estimates relative to lidar measurements (R^2 = 0.71). This strong linear trend resulted in a greater dominance of systematic (RMSEs = 15%) over unsystematic, or random noise (RMSEU =9%) errors in the Landsat estimates compared to MODIS, suggesting a greater potential for empirical calibration of Landsat estimates than is possible for the MODIS dataset. Although still present, saturation of Landsat estimates relative to lidar measurements was reduced slightly compared to the saturation seen in MODIS-based estimates. Landsat estimates reproduced the spatial pattern of tree cover in most sites with greater fidelity than did MODIS estimates. Landsat estimates resolved greater spatial variation in tree cover than did the relatively coarse MODIS estimates.

5.2. Validation: Forest Cover and Change

5.2.1. Method

5.2.1.1. Sampling Design

Accuracy assessment employed a two-stage, stratified sampling design (Cochran, 1977, Sannier et al. 2014, Särndal et al. 1992, Stehman, 1999, Stehman & Czaplewski, 1998). To increase the representation of rare classes, reference data were sampled across the global land area in two stages, first selecting Landsat WRS-2 tiles within predefined global strata and then sampling pixels within each selected tile. The spatial location of sample points was held constant for all time periods.

5.2.1.2. Biome Definition

Biome-level stratification was based on the 16 major habitat types delineated by the Nature Conservancy (TNC) Terrestrial Ecoregions of the World dataset (TNC, 2012). Excluding deserts and xeric shrublands, inland water, and rock & ice, we merged the major habitat types into eight forest and non-forest biomes (Table 8). Among the 7,277 WRS-2 tiles in the 8 biomes, the 5,294 tiles completely contained within biome were assigned to their respective biomes, and tiles spanning biome boundaries (including land/ocean boundaries) were excluded. This reduced the land area for each of the eight biomes available for sampling by 18.7 - 58.2% for each biome (Table 8).

Table 8. Reclassification of TNC major habitat types (TNC, 2012) into biome strata. The land area for each biome is reported in the "Land area (km^2)" column, and the percentage of that area reduced by excluding tiles spanning boundaries is reported in "Spanning biome WRS-2 tiles (%)" column. The percentage of edge pixels is reported in the "Edge pixels (%)" column.

Biome Strata	TNC Biomes	Land Area (km^2)	% Reduction (WRS-2 Tile Spanning Biomes)	% Reduction (Edge Pixels)
Tropical Evergreen Forests	Tropical and Subtropical Moist Broadleaf Forest Mangroves Tropical and Subtropical Coniferous Forests	16,608,638	25.2	9.7
Tropical Deciduous Forests	Tropical and Subtropical Dry Broadleaf Forests	6,780,454	18.7	8.4
Tropical Non-forest	Tropical and Subtropical Grasslands, Savannas, and Shrublands	15,296,731	28.0	5.5

	Flooded Grasslands and Savannas (23° S – 23°N) and Montane Grasslands and Shrublands (23° S – 23°N)			
Temperate Evergreen Forests	Temperate Conifer Forests	3,843,538	50.9	13.2
Temperate Deciduous Forests	Temperate Broadleaf and Mixed Forests Mediterranean Forests, Woodlands, and Scrub	14,013,894	29.1	9.4
Temperate Non-Forest	Temperate Grasslands, Savannas, and Shrublands Flooded Grasslands and Savannas (23° S – 23°N) and Montane Grasslands and Shrublands (23° S – 23°N)	2,918,100	58.2	2.0
Boreal Forests	Boreal Forests/Taiga	20,381,706	24.9	12.3
Boreal Non-forest	Tundra	21,484,150	21.1	3.8
[Excluded]	Deserts and Xeric Shrublands Inland Water			

5.2.1.3. Response Design

Forest or non-forest cover in each pixel and each epoch was visually identified by experienced image analysts using a web-based tool presenting the GLS Landsat image(s) covering each location, as well as auxiliary information, including: Normalized Difference Vegetation Index (NDVI) phenology from MODIS, high-resolution satellite imagery and maps from Google Maps, and geotagged ground photos (Figure 16) (Feng et al., 2012b). The Landsat images were presented in multiple 3-band combinations—e.g., near infrared (NIR)- red (R)-green (G), R-G-blue (B), and shortwave infrared (SWIR)-NIR-R. The extent of each selected 30-m Landsat pixel was extracted in the Universal Transverse Mercator (UTM) coordinate system and delineated in both the Landsat image and in Google Maps to facilitate visual comparison. The NDVI profile was derived from the 8-day composited surface reflectance data (MOD09A1; Vermote & Kotchenova 2008; Vermote et al. 2002)with nearest-neighbor interpolation, excluding data labeled as cloud or shadow in the MOD09A1 Quality Assurance (QA) layer (Feng et al., 2012b).

The selected points were randomly distributed among 12 experts for interpretation (Table 9). Experts visually checked the information provided by the tool and labeled each point either “forest” or “non-forest” for each of the 3 epochs individually. Points with Landsat pixels contaminated with cloud or shadow were labeled as “cloud” and “shadow” respectively. If an expert was unable to identify the cover of a pixel, he or she was instructed to label it as “unknown” for further investigation.

Over 1,000 collected points were located in each decile of tree cover, with nearly uniform sample size across the range of tree cover > 10% cover. Of these points, > 90% were labeled as forest or non-forest by visual interpretation of TM or ETM+ images in the 1990, 2000, and 2005 epochs, with only 6 % of the points remaining as “unknown”. Less than 1 % of the points across all epochs were interpreted as “cloud” or “shadow”. The distribution of the unknown points in the 2000 epoch revealed that these difficult points were rare (< 4 %) in areas of low or high tree-canopy cover but were much more frequent in areas with 5 – 35 % tree cover.

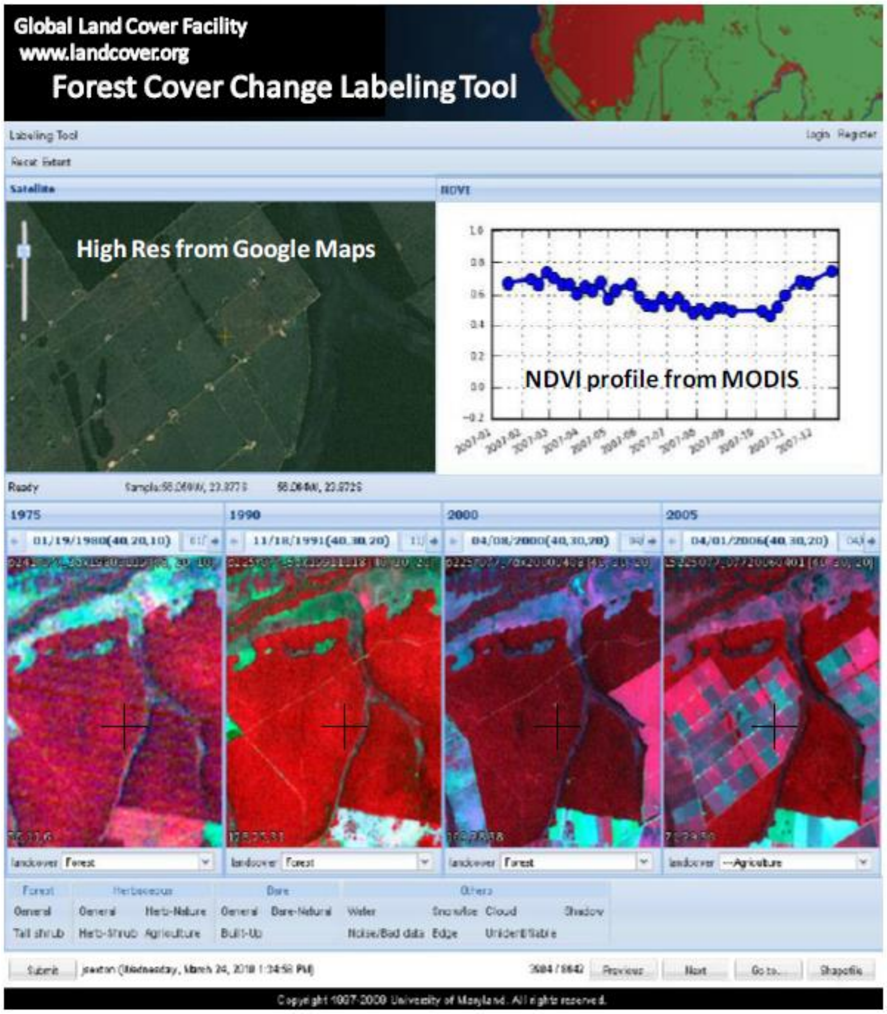

Figure 16. The web-based tool for visually identifying forest cover at a selected point (Feng et al. 2012).

Table 9. Sample sizes of human-interpreted reference data for circa1990, 2000, and 2005 epochs.

Type	Number of points		
	1990	**2000**	**2005**
Nonforest	10,657	11,244	11,929
Forest	15,221	15,194	14,448
Unknown	2,025	1,543	1,494
Cloud	9	26	30
Shadow	30	28	28

5.2.1.4. Validation Metrics

Based on the independent reference sample, the labeled points were used to quantify the accuracy of the global forest-cover and -change layers using validation metrics weighted by area

(Card 1982; Congalton 1991; Stehman & Czaplewski 1998; Stehman 2014). For each reference datum, i, the agreement between estimated and reference coveror change, y, was defined:

$$y_i = \begin{cases} 1 & \text{if } \hat{c}_i = c_i \\ 0 & \text{if } \hat{c}_i \neq c_i \end{cases}. \tag{38}$$

Weights were applied to the data to remove the effect of disproportional sampling, by standardizing the inclusion probability of each observation proportional to the area of each stratum (Sexton et al., 2013b). Each point's weight, , was calculated as the inverse of the joint standardized probability of its selection at the tile- and pixel-sampling stages:

$$w_i = \frac{P(i|S)}{p(i|S)} \frac{P(T|G)}{p(T|G)} = \left(\frac{n_S}{N_S} \div \frac{n_i}{N_i}\right)\left(\frac{n_G}{N_G} \div \frac{n_T}{N_T}\right)\cos(\varphi_i), \tag{39}$$

elements of the diagonal of the confusion matrix—divided by the weighted total number of points ( ):

$$\mathrm{OA} = \sum_{\mathrm{i=1}}^{\mathrm{n_a}} \mathrm{y_i} \times \mathrm{w_i} \Big/ \sum_{\mathrm{i=1}}^{\mathrm{n_a}} \mathrm{w_i}. \tag{40}$$

The conditional probability of the estimate given the reference (i.e., human-interpreted) class, P(c|ĉ) (i.e., User's Accuracy, UA) and the conditional probability of the reference class given the estimate P(ĉ|c) (i.e., Producer's accuracy, PA) were calculated as:

$$\mathrm{CE_c} = 1\text{-}\mathrm{UA_c} = 1\text{-} \sum_{\mathrm{i=1}}^{\mathrm{n_{\hat{c}}}} \mathrm{y_i} \times \mathrm{w_i} \Big/ \sum_{\mathrm{i=1}}^{\mathrm{n_{\hat{c}}}} \mathrm{w_i} \tag{41}$$

$$\mathrm{OE_c} = 1\text{-}\mathrm{PA_c} = 1\text{-} \sum_{\mathrm{i=1}}^{\mathrm{n_c}} \mathrm{y_i} \times \mathrm{w_i} \Big/ \sum_{\mathrm{i=1}}^{\mathrm{n_c}} \mathrm{w_i}, \tag{42}$$

where $\hat{n}$ were the points identified as type c (e.g., forest, non-forest, forest gain, or forest loss) by the GLCF layers, and nc were the points identified as type c by the reference (Stehman, 2014). The inverse of P(c|ĉ) and P(ĉ|c) were interpreted as errors of commission and omission respectively.

The variance of the accuracy metrics is described below. The points in each forest/non-forest status stratum were randomly selected. Hence, the variance of the OA for the stratum and the UA and PA of class c (i.e., forest and non-forest for forest cover; FF, FN, NF, and NN for forest-cover change) in the stratum were calculated following (Congalton and Green 2010, p116-119; Olofsson et al. 2014):

$$v(\widehat{OA}) = \frac{1}{\sum_{i=1}^{n} n_{+i}^2} \sum_{i=1}^{n} n_{+i}^2 \, \widehat{UA}_i \frac{(1-\widehat{UA}_i)}{n_{i+}-1} \tag{43}$$

$$v(\widehat{UA}_c) = \widehat{UA}_c \frac{(1-\widehat{UA}_c)}{n_{c+}-1} \tag{44}$$

$$v(\widehat{PA}_c) = \frac{1}{\sum_{k=1}^{n} \frac{n_{+k}}{n_{k+}} n_{kc}} \left[\frac{n_{+c}^2(1-\widehat{PA}_c)^2 \widehat{UA}_c(1-\widehat{UA}_c)}{n_{c+}-1} + \widehat{PA}_c^2 \sum_{i \neq c}^{n} \frac{n_{+i}^2 \frac{n_{ic}}{n_{i+}}\left(1-\frac{n_{ic}}{n_{i+}}\right)}{(n_{i+}-1)}\right], \tag{45}$$

where was the number of points in the error matrix at cell (i, j), and +and + were respectively the summaries of rows (i) and columns (j) in the matrix.

The estimated variances (( )) for the accuracy metrics (i.e., OA, UA, and PA) of the globe and each biome were calculated following (Cochran 1977):

$$v(\hat{\theta}) = \sum_{k=1}^{n_G} \left(\frac{A_k}{\sum_{l=1}^{n_G} A_l} \right)^2 \left[\frac{1}{n_G} \sum_{j=1}^{n_T} W_j \left(\hat{\theta}_j - \hat{\bar{\theta}}_j \right)^2 + \sum_{i=1}^{n_j} W_{ij}^2 \, v(\hat{\theta}_{ij}) \right] \quad (46)$$

where a biome (G) consisted of biome-change strata. Each biome-change stratum (k) covered area and included selected WRS-2 tiles. The weight for each tile (j) was calculated as:

$$W_j = \frac{\cos(\varphi_j)}{\sum_{i=1}^{n_T} \cos(\varphi_i)}, \quad (47)$$

where is the central latitude of tile (j). A tile (j) consisted of forest status strata, and the accuracy for the tile ( ) was estimated:

$$\hat{\theta}_j = \sum_{i=1}^{n_j} W_{ij} \, \hat{\theta}_{ij}, \quad (48)$$

where was the weight for a forest status stratum (i) within tile (j):

$$W_{ij} = \frac{N_{ij}}{\sum_{i=1}^{n_j} N_{ij}}, \quad (49)$$

where was the number of pixels in stratum (i) of tile (j). The mean ( ) of accuracy ( ) for tile (j) was calculated:

$$\hat{\bar{\theta}}_j = \sum_{j=1}^{n_T} W_j \, \hat{\theta}_j. \quad (50)$$

The standard error (SE) of each accuracy metric was calculated as the square root of its varianc

$$SE(\hat{\theta}) = \sqrt{v(\hat{\theta})}. \quad (51)$$

5.2.1.5. Accuracies of Forest Cover Layers

Accuracy of forest-cover detection was consistently high across all biomes and epochs, with OA = 91% (SE≈1%) in each of the 1990, 2000, and 2005 layers (Figure 11, Table 10). Commission errors (CE = 1 - P(c|ĉ)) and omission errors (OE = 1 - P(ĉ|c)) were < 10% for both forest and non-forest classes in all epochs, for which SE < 2.3%. The original, unadjusted estimates showed a bias toward detection of non-forest, with the forest class having a higher rate of omission errors (<21%) than commission errors (<3%) and the non-forest class having a higher rate of commission errors (<13%) than omission errors (<2%) in all epochs and biomes.

The largest overall accuracies (OA) were found in temperate forest and non-forest, tropical evergreen, and boreal non-forest biomes—each of which had OA > 90% (SE < 5%). OA were slightly lower in boreal forests (83% < OA < 89%); OA of tropical deciduous forest ranged from 80.7% to 84%; and OA of tropical non-forest ranged from 83.2% to 84.1%. Standard errors of OA were lowest (<1.6%) in evergreen forests and temperate nonforest, slightly higher in deciduous and boreal forest (<2.9%), and highest in boreal and tropical nonforest (<5%). Evergreen and boreal forests had the lowest rate of omission error (OE < 21%; SE < 3.5%) for the forest class, followed by deciduous forests (24% < OE < 55%; SE < 9.6%) and non-forest biomes (59% < OE; SE < 7.6%). The non-forest class had low omission error (OE < 10%; SE < 8.5%) in all biomes, and its commission error rate was larger in the forest biomes (≤ 32.3%; SE < 6.3%) than the non-forest biomes (≤ 18.3%; SE < 3.3%).

These estimates of accuracy are likely conservative, given our exclusion of treeless biomes and the uncertainty of reference data generated by identifying forest cover by visual interpretation of satellite images (Montesano et al., 2009; Sexton et al., 2015a). Montesano et al. (2009) found that human experts achieved 18.7% RMSE in visual estimation of tree cover in high-resolution imagery, and Sexton et al. (2015a) found that visual confusion was greatest near the threshold of tree cover used to define forests, especially when interpreting change. To investigate the relation between accuracy and tree cover, OA of forest/non-forest cover in 2000 was plotted over the range of coincident tree cover estimated by the NASA GFC tree-cover dataset (Sexton et al., 2013a). A distinct concavity was evident in the relation, which reached its minimum near the 30% tree-cover threshold used to define forests. The OA was large (> 80%) where tree cover was < 0.1 or > 0.35. Commission and omission errors were also investigated in relation with tree cover (Figure 20). Commission error of the forest class was < 10% except among pixels with tree cover < 0.35, where the commission error was < 20%. Omission error of forest was < 20% in areas with > 0.4 tree cover but increased in areas of sparse tree cover.

5.2.1.6. Accuracies of Forest Change Layers

Globally, overall accuracy (OA) of the 1990-2000 forest-change layer equaled 88.1% (SE = 1.19%), and OA = 90.2% (SE = 1.1%) for the 2000-2005 forest-change layer (Table 12). In each period and biome, OA ≥ 78.7% (SE < 5%). The global accuracies and standard errors of stable forest (FF) and stable non-forest (NN) classes were similar respectively to those of the stable forest and non-forest classes in the 1990, 2000, and 2005 layers, but the change classes—i.e., forest loss (FN) and forest gain (NF)—had larger error rates than the static classes in the respective epochs.

Commission and omission errors for forest loss were between 45% and 62% globally, with SE between 1.72% and 23.48%. Forest-loss was detected most accurately, with errors dominated by commission, in temperate and tropical evergreen forest biomes (PA ≥ 71.7%; UA ≥ 49.6%). This was likely due to relatively minimal impact of vegetation phenology on canopy reflectance in evergreen forests. Whether in temperate or tropical regions, detection of forest loss was more accurate in evergreen forests than in their deciduous counterparts (30% ≤ PA < 39%; 36.1% ≤ UA ≤ 50.1%). In non-forest biomes, accuracy of forest-loss detection was very low and dominated by omissions, but the rarity of forests and their loss in these biomes made the impact of these errors on overall accuracy small.

Forest gain was consistently the most difficult dynamic to detect, with OE and CE each > 60% in all epochs (SE < 17%). This was likely due to the long traversal of intermediate tree cover during canopy recovery from disturbance, compounded by the uncertainty of human identification of change (Sexton et al. 2015a). Producer's accuracies tended to be largest in tropical evergreen forests (24.9% ≤ PA ≤ 75.7%), where canopy recovery following disturbance is fastest, and smallest in non-forest biomes (PA < 19%; UA < 17%), where recovery is slower and locations spend more time in intermediate ranges of canopy cover.

The effect of tree cover on accuracy was investigated using the 2000-2005 forest change layer. Similar to that of the 2000 forest-cover layer, a distinct concavity was evident in the relationship between overall forest-change accuracy and tree cover, and accuracy was lowest between 0.2-0.3 tree cover. Commission and omission errors of stable forest and non-forest in relation to tree cover were similar to those of forest and non-forest in the static layers. The commission and omission errors were large in areas with tree cover < 0.35 and decreased to < 60% in areas with tree cover > 0.35. Commission and omission errors of forest gain were both correlated to tree cover. The omission error was < 45% and commission error was < 70% in areas with 0.3 - 0.6 tree cover but > 50% in high or low tree cover.

Table 10. Percent accuracies of the 1990, 2000, and 2005 forest-cover layers relative to human- interpreted reference points. The standard error associated with each accuracy is reported in brackets.

	1990		2000		2005	
Type	$P(c\|\hat{c})$	$P(\hat{c}\|c)$	$P(c\|\hat{c})$	$P(\hat{c}\|c)$	$P(c\|\hat{c})$	$P(\hat{c}\|c)$
F	97.2 (1.99)	79.8 (1.05)	98.2 (1.24)	79.9 (1.09)	97.9 (1.15)	79.8 (1.06)
N	87.8 (1.93)	98.5 (1.10)	87.6 (2.28)	99.0 (1.19)	87.9 (2.20)	98.8 (1.44)
OA	90.9 (1.03)		91.1 (0.96)		91.2 (1.01)	

6. Caveats/Known Issues

7. References

Ackerman, SA, CC Moeller, LE Gumley, KI Strabala, WP Menzel & RA Frey. 1998. Discriminating clear sky from clouds with MODIS. Journal of Geophysical Research D: Atmospheres 103:32141-32157.

Asner, GP, DE Knapp, EN Broadbent, PJC Oliveira, M Keller & JN Silva. 2005. Selective Logging in the Brazilian Amazon. Science 310:480-482.

Band, LE. 1993. Effect of land surface representation on forest water and carbon budgets. Journal of Hydrology 150:749-772.

Borak, JS. 1999. Feature selection and land cover classification of a MODIS-like data set for a semiarid environment. International Journal of Remote Sensing 20:919-938.

Bounoua, L, H Khan, R Defries, GJ Collatz & P Sellers. 2002. Effects of land cover conversion on surface climate. Climatic Change 52:29-64.

Carpenter, GA, S Gopal, S Macomber, S Martens & CE Woodcock. 1999. A neural network method for mixture estimation for vegetation mapping. Remote Sensing of Environment 70:138-152.

Chander, G & B Markham. 2003. Revised Landsat-5 TM Radiometric Calibration Procedures and Postcalibration Dynamic Ranges. IEEE Transactions on Geoscience and Remote Sensing 41:2674-2677.

Chander, G, BL Markham & DL Helder. 2009. Summary of current calibration coefficients for Landsat MSS, TM, ETM+, and EO-1 ALI sensors. Remote Sensing of Environment 113:893-903.

Channan, S, M Feng, D-H Kim, JO Sexton, X-P Song, D Song, P Noojipady, K Collins, A Anand & JR Townshend. 2015. The GLS+: an enhancement of the Global Land Survey datasets. Photogrammetric Engineering & Remote Sensing 81:521-525.

Clark, JS. 2007. Models for Ecological Data: An Introduction. Princeton University Press. 632 pp.

Cochran, WG. (1977). Sampling Techniques (3rd editio). New York: John Wiley & Sons.

Cook, BD, PV Bolstad, E Naesset, RS Anderson, S Garrigues, JT Morissette, J Nickeson & KJ Davis. 2009. Using LiDAR and quickbird data to model plant production and quantify uncertainties with wetland detection and land cover generalizations. Remote Sensing of Environment 113: 2366-2379.

DeFries, RS, L Bounoua, CB Field, I Fung & GJ Collatz. 1999. Combining satellite data and biogeochemical models to estimate global effects of human-induced land cover change on carbon emissions and primary productivity. Global Biogeochemical Cycles 13:803-815.

DeFries, RS, RA Houghton, MC Hansen, CB Field, D Skole & J Townshend. 2002. Carbon emissions from tropical deforestation and regrowth based on satellite observations for the 1980s and 1990s. Proceedings of the National Academy of Sciences 99:14256-14261.

DiMiceli, CM, ML Carroll, RA Sohlberg, C Huang, MC Hansen & JRG Townshend. 2011. MODIS Vegetation Continuous Fields (MOD44B) Percent Tree Cover Dataset. University of Maryland, College Park, MD.

Dubayah, RO, SL Sheldon, DB Clark, MA Hofton, JB Blair, GC Hurtt & RL Chazdon. 2010. Estimation of tropical forest height and biomass dynamics using lidar remote sensing at La Selva, Costa Rica. Journal of Geophysical Research 115:G00E09

Dudley, N, D Baldock, R Nasi & S Stolton. 2005. Measuring biodiversity and sustainable management in forests and agricultural landscapes. Philosophical Transactions of the Royal Society of London B 360:457.

FAO 2001. Global forest resources assessment 2000 -- main report. FAO Forestry Paper 140, Rome: Food and Agriculture Organization of the United Nations.

Feng, M, C Huang, S Channan, EF Vermote, JG Masek & JR Townshend. 2012. Quality assessment of Landsat surface reflectance products using MODIS data. Computers & Geosciences 38:9-22.

Feng, M, JO Sexton, C Huang, JG Masek, EF Vermote, F Gao, R Narasimhan, S Channan, RE Wolfe & JR Townshend. 2013. Global, long-term surface reflectance records from Landsat: a comparison of the Global Land Survey and MODIS surface reflectance datasets. Remote Sensing of Environment 134:276-293

Feng, M, JO Sexton, S Channan, JR Townshend. 2015. A global, high-resolution (30-m) inland water body dataset for 2000: first results of a topographic-spectral classification algorithm. International Journal of Digital Earth. DOI: 10.1080/17538947.2015.1026420

Fortier, J, J Rogan, CE Woodcock & RD Miller. 2011. Utilizing temporally invariant calibration sites to classify multiple dates and types of satellite imagery. Photogrammetric Engineering and Remote Sensing 77:181-189.

Franks, S, JG Masek, RMK Headley, J Gasch & T Arvidson. 2009. Large Area Scene Selection Interface (LASSI). Photogrammetric Engineering and Remote Sensing 11:1287-1296.

Gao, F, J Masek, J & R Wolfe. 2009. An automated registration and orthorectification package for Landsat and Landsat-like data processing. Journal of Applied Remote Sensing 3:033515. doi: 10.1117/1.3104620.

Gao, F, J Masek, M Schwaller & F HalL. 2006. On the blending of the Landsat and MODIS surface reflectance: predicting daily Landsat surface reflectance. IEEE Transactions on Geoscience and Remote Sensing 44:2207-2218.

GCOS. 2004. Implementation plan for the Global Observing System for climate in support of the UNFCCC. GCOS - 92 (WMO/TD No. 1219), Geneva: Global Climate Observing System.

Gray, J, & C Song. 2013. Consistent classification of image time series with automatic adaptive signature generalization. Remote Sensing of Environment 134:333-341.

Gutman, G, R Byrnes, J Masek, S Covington, C Justice, S Franks & R Headley. 2008. Towards monitoring changes at a global scale: the Global Land Survey. Photogrammetric Engineering and Remote Sensing 74: 6-10.

Hall, FG, DE Stebel, JE Nickeson & SJ Goetz. 1991. Radiometric rectification: toward a common radiometric response among multidate, multisensor images. Remote Sensing of Environment 35:11-27.

Hansen, MC, PV Potapov, R Moore, M Hancher. SA Turubanova, A Tyukavina, & JRG Townshend. 2013. High-Resolution Global Maps of 21st-Century Forest Cover Change. Science 342:850-853.

Hansen, MC, RS DeFries, JRG Townshend, L Marufu & R Sohlberg. 2002. Development of a MODIS tree cover validation data set for Western Province, Zambia. Remote Sensing of Environment 83:320.

Hansen, MC, RS DeFries, JRG Townshend, M Carroll, C Dimiceli & RA Sohlberg. 2003. Global Percent Tree Cover at a Spatial Resolution of 500 Meters: First Results of the MODIS Vegetation Continuous Fields Algorithm. Earth Interactions 7:1–15.

Hastie, T, R Tibshirani & R Friedman. 2001. Elements of Statistical Learning: Data Mining, Inference, and Prediction. Springer-Verlag.

Heiskanen, J. 2008. Evaluation of global land cover data sets of the tundra-taiga transition zone in northernmost Finland. International Journal of Remote Sensing 29:3727-3751.

Holben, BN, TF Eck, I Slutsker, D Tanré, JP Buis, A Setzer, E Vermote, JA Reagan, YJ Kaufman, T Nakajima, F Lavenu, I Jankowiak & A Smirnov. 1998. AERONET—A federated instrument network and data archive for aerosol characterization. Remote Sensing of Environment 66:1-16

Homer, C, C Huang, L Yang, B Wylie & M Coan. 2004. Development of a 2001 national land cover database for the United States. Photogrammetric Engineering & Remote Sensing 70:829-840.

Houghton, RA 1998. Historic role of forests in the global carbon cycle. In: GH Kohlmaier, M Weber & RA Houghton (eds.) Carbon dioxide mitigation in forestry and wood industry (pp. 1-24), Berlin: Springer.

Huang, C, K Song, S Kim, JRG Townshend, P Davis, J Masek & SN Goward. 2008. Use of a Dark Object Concept and Support Vector Machines to Automate Forest Cover Change Analysis. Remote Sensing of Environment 112:970-985.

Huang, C, N Thomas, SN Goward, J Masek, Z Zhu, JRG Townshend & JE Vogelmann. 2010. Automated Masking of Cloud and Cloud Shadow for Forest Change Analysis. International Journal of Remote Sensing 31:5449-5464.

Huang, C, S Kim, A Altstatt, JRG Townshend, P Davis, K Song, CJ Tucker, O Rodas, A Yanosky, R Clay & J Musinsky. 2007. Rapid loss of Paraguay's Atlantic forest and the status of protected areas – a Landsat assessment. Remote Sensing of Environment 106:460-466.

Hyde, P, R Dubayah, B Peterson, JB Blair, M Hofton, C Hunsaker, R Knox & W Walker. 2005. Mapping forest structure for wildlife habitat analysis using waveform lidar: Validation of montane systems. Remote Sensing of Environment 96: 427-437.

International Geosphere-Biosphere Programme (IGBP). 1992, Improved Global Data for Land Applications. IGBP Global Change Report No. 20, edited by JRG Townshend. International Geosphere Biosphere Programme, Stockholm, Sweden

Irish, RR. 2000. Landsat 7 Automatic Cloud Cover Assessment. In: Proceedings of SPIE: Algorithms for Multispectral, Hyperspectral, and Ultraspectral Imagery VI. April 24-26, 2000, Orlando, U.S.A. 348-355.

Kaufman, YJ, AE Wald, LA Remer, et al. 1997. The MODIS 2.1-micron channel Œ correlation with visible reflectance for use in remote sensing of aerosol. IEEE Transactions on Geoscience & Remote Sensing 35:1286-1296.

Kellner, JR, DB Clark, & MA Hofton. 2009. Canopy height and ground elevation in a mixed-land-use lowland Neotropical rain forest landscape. Ecological Archives E090-233.

Kim, D-H, JO Sexton, P Noojipady, C Huang, A Anand, S Channan, M Feng & JR Townshend. 2014. Global, Landsat-based forest-cover change from 1990 to 2000. Remote Sensing of Environment 155: 178-193.

Kim, D-H, R Narasimhan, JO Sexton, C Huang & JR Townshend. 2011. Methodology to select phenologically suitable Landsat scenes for forest change detection. IEEE International Geoscience and Remote Sensing Symposium (IGARSS), 2613-2616. Vancouver, Canada.

Korhonen, L, I Korpela, J Heiskanen, & M Maltamo. 2011. Airborne discrete-return LIDAR data in the estimation of vertical canopy cover, angular canopy closure and leaf area index. Remote Sensing of Environment 115:1065–1080.

Kotchenova, SY, EF Vermote, R Matarrese, & F Klemm, 2006. Validation of a new vector version of the 6S radiative transfer code for atmospheric correction of MODIS data: Part I – Path Radiance. Applied Optics 45:6762-6774.

Lal, R. 1995. Sustainable management of soil resources in the humid tropics (146 pp.), New York: United Nations University Press.

Lepers, E, EF Lambin, AC Janetos, R DeFries, F Achard, N Ramankutty, & RJ Scholes. 2005. A synthesis of information on rapid land-cover change for the period 1981-2000. BioScience 55:115-124.

Markham, BL, R Morfitt, JL Barker, E Kaita, & J Seiferth. 2003. On-orbit performance of the Landsat-7 ETM + radiometric calibrators. International Journal of Remote Sensing 24:265-285.

Masek, JG, EF Vermote, NE Saleous, R Wolfe, FG Hall, KF Huemmrich, G Feng, J Kutler, & L Teng-Kui. 2006b. A Landsat surface reflectance dataset for North America, 1990-2000. IEEE Geoscience and Remote Sensing Letters 3:68-72.

Masek, JG, M Friedl, T Loveland, E Brown de Colstoun, J Townshend, M Hansen, & KJ Ranson. 2006a.ESDR Community White Paper on Land Cover/Land Cover Change. NASA, Greenbelt, MD, pp. 9.

Matthews E & A Grainger. 2002. Evaluation of FAO's Global Forest Resources Assessment from the user perspective. Unasylva 210: 42-55.

McFeeters, SK 1996. The use of Normalized Difference Water Index (NDWI) in the delineation of open water features. International Journal of Remote Sensing 17:1425-1432.

McIver, DK & MA Friedl. 2002. Using prior probabilities in decision-tree classification of remotely sensed data. Remote Sensing of Environment 81: 253-261.

Montesano, PM, R Nelson, G Sun, H Margolis, A Kerber & KJ Ranson. 2009. MODIS tree cover validation for the circumpolar taiga–tundra transition zone. Remote Sensing of Environment 113: 2130–2141.

Muchoney, DM & BN Haack. 1994. Change detection for monitoring forest defoliation. Photogrammetric Engineering & Remote Sensing 60:1243-1251.

Ojima, DS & KA Galvin. 1994. The global impact of land-use change. BioScience 44:300 - 304.

Olson, DM, E Dinerstein, ED Wikramanayake, ND Burgess, GVN Powell, EC Underwood, JA D'amico, I Itoua, HE Strand, JC Morrison, CJ Loucks, TF Allnutt, TH Ricketts, Y Kura, JF Lamoreux, WW Wettengel, P Hedao & KR Kassem. 2001. Terrestrial ecoregions of the world: a new map of life on Earth. Bioscience 51:933–938.

Olsson, H. 1994. Changes in satellite-measured reflectances caused by thinning cuttings in boreal forest. Remote Sensing of Environment 50:221-230.

Pandey, DN. 2002. Sustainability science for tropical forests. Conservation Ecology 6:13.

Pax-Lenney, M, CE Woodcock, SA Macomber, S GopaL & C Song. 2001. Forest mapping with a generalized classifier and Landsat TM data Remote Sensing of Environment 77:241-250.

Pittman, K, MC Hansen, I Becker-Reshef, PV Potapov & CO Justice. 2010. Estimating global cropland extent with multi-year MODIS data. Remote Sensing 2:1844-1863.

Quinlan, JR. 1986. Induction of decision trees. Machine Learning 1:81-106.

Quinlan, JR. 1993. C4.5: Programs for Machine Learning. San Francisco, CA. Morgan Kaufmann.

Remer, LA, YJ Kaufman, D Tanré, S Mattoo, DA Chu, JV Martins, R-R Li, C Ichoku, RC Levy, RG Kleidman, TF Eck, E Vermote & BN Holben. 2005. The MODIS Aerosol Algorithm, Products and Validation. Journal of Atmospheric Sciences 62:947-973.

Sahin, V & MJ Hall. 1996. The effects of afforestation and deforestation on water yields. Journal of Hydrology 178:293-309.

Sannier, C, RE McRoberts, L-V Fichet, E Massard, & K Makaga. 2014. Using the regression estimator with Landsat data to estimate proportion forest cover and net proportion deforestation in Gabon. Remote Sensing of Environment 151:138–148.

Särndal, C-E, B Swensson, & JH Wretman. 1992. Model assisted survey sampling. New York: Springer-Verlag New York.

Sexton, JO, DL Urban, MJ Donohue & C Song. 2013c. Long-term land cover dynamics by multi-temporal classification across the Landsat-5 record. Remote Sensing of Environment 128:246-258.

Sexton, JO, P Noojipady, A Anand, X-P Song, C Huang, SM McMahon, M Feng, S Channan & JR Townshend. 2015. A model for the propagation of uncertainty from continuous estimates of tree cover to categorical forest cover and change. Remote Sensing of Environment 156: 418-425.

Sexton, JO, P Noojipady, XP Song, M Feng, DX Song, DH Kim, A Anand, C Huang, S Channan, SL Pimm, JR Townshend. 2016. Conservation policy and the measurement of forests. Nature Climate Change 6:192-196.

Sexton, JO, RD Ramsey & DL Bartos. 2006. Habitone analysis of quaking aspen in the Utah Book Cliffs: effects of site water demand and conifer cover. Ecological Modelling 198: 301-311.

Sexton, JO, X-P Song, C Huang, S Channan, ME Baker & JR Townshend. 2013a. Urban growth of the Washington, D.C. – Baltimore, MD metropolitan region from 1984 to 2010 by annual estimates of impervious cover. Remote Sensing of Environment 129:42-53.

Sexton, JO, X-P Song, M Feng, P Noojipady, A Anand, C Huang, D-H Kim, KM Collins, S Channan, C DiMiceli & JR Townshend. 2013b. Global, 30-m resolution continuous fields of tree cover: Landsat-based rescaling of MODIS continuous fields and lidar-based estimates of error. International Journal of Digital Earth 6: 427-448.

Skole, D & C Tucker. 1993. Tropical deforestation and habitat fragmentation in the Amazon: satellite data from 1978 to 1988. Science 260:1905-1910.

Skole, DL, CO Justice, JRG Townshend & AC Janetos. 1997. A land cover change monitoring program: strategy for an international effort. Mitigation and Adaptation Strategies for Global Change 2:157-175.

Skole, DL, WA Salas & V Taylor. 1998. Global Observation of Forest Cover: fine resolution data and product design strategy, report of a workshop, Paris, France: CNES.

Snedecor, GW & WG Cochran. 1989. Statistical Methods, 8th ed. Iowa State University Press. Ames, Iowa.

Song, X, C Huang, JO Sexton, M Feng, R Narasimhan, S Channan & JR Townshend. 2011. An assessment of global forest cover maps using regional higher-resolution reference datasets. Proceedings of IEEE International Geoscience and Remote Sensing Symposium pp. 752–755.

Stehman, SV & RL Czaplewski. 1998. Design and Analysis for Thematic Map Accuracy Assessment - an application of satellite imagery. Remote Sensing of Environment 64:331–344.

Stehman, SV. 1999. Basic probability sampling designs for thematic map accuracy assessment. International Journal of Remote Sensing 20:2423–2441.

Stehman, SV. 2014. Estimating area and map accuracy for stratified random sampling when the strata are different from the map classes. International Journal of Remote Sensing 35:37–41.

Steininger, MK, A Desch, V Bell, P Ernst, CJ Tucker, JRG Townshend & TJ Killeen. 2001. Tropical Deforestation in the Bolivian Amazon. Environmental Conservation 28:127-134.

Strahler, AH. 1980. The use of prior probabilities in maximum likelihood classification of remotely sensed data. Remote Sensing of Environment 10:135-163.

Tachikawa, T, M Hato, M Kaku, A Iwasaki. 2011. Characteristics of ASTER GDEM version 2. IEEE Geoscience and Remote Sensing Symposium. 2011.

Townshend, JR & MA Brady. 2006. A Revised Strategy for GOFC-GOLD: GOFC-GOLD.

Townshend, JR, CO Justice, DL Skole, A Belward, A Janetos, I Gunawan, JG Goldammer & B Lee. 2004. Meeting the Goals of GOFC. In: Gutman, G, AC Janetos, CO Justice, EF Moran, JF Mustard, RR Rindfuss, D Skole, BL Turner II & MA Cochrane (eds.) Land Change Science (pp. 31 - 51), Dordrecht: Kluwer Academic Publishers.

Townshend, JR, JG Masek, C Huang, EF Vermote, F Gao, S Channan, JO Sexton, M Feng, R Narasimhan, D-H Kim, K Song, D Song, X Song, P Noojipady, B Tan, MC Hansen, M Li & R Wolfe. 2012. Global characterization and monitoring of forest cover using Landsat data: opportunities and challenges. International Journal of Digital Earth 5:373-397.

Townshend, JRG & CO Justice. 1988. Selecting the spatial resolution of satellite sensors required for global monitoring of land transformations. International Journal of Remote Sensing 9:187-236.

Tucker, CJ & JRG Townshend. 2000. Strategies for monitoring tropical deforestation using satellite data. International Journal of Remote Sensing 21:1461-1471.

Tucker, CJ, DM Grant & JD Dykstra. 2004. NASA's Global Orthorectified Landsat Data Set. Photogrammetric Engineering & Remote Sensing 70:313-322.

Tucker, CJ, JE Pinzon, ME Brown, D Slayback, EW Pak, R Mahoney, E Vermote & NE Saleous. 2005. An Extended AVHRR 8-km NDVI Data Set Compatible with MODIS and SPOT Vegetation NDVI Data. International Journal of Remote Sensing 26:4485-4498

USGCRP. 1999. A U.S. Carbon Cycle Science Plan, Washington, D.C.: U.S. Global Change Research Program.

Vermote, EF & S Kotchenova. 2008. Atmospheric correction for the monitoring of land surfaces. Journal of Geophysical Research 113:D23S90

Vermote, EF, N El Saleous, CO Justice, YJ Kaufman, JL Privette, L Remer, JC Roger & D Tanré. 1997. Atmospheric correction of visible to middle-infrared EOS-MODIS data over land surfaces: background, operational algorithm and validation. Journal of Geophysical Research 102:17131-17141.

Vermote, EF, NZ El Saleous & CO Justice. 2002. Atmospheric correction of MODIS data in the visible to middle infrared: first results. Remote Sensing of Environment 83:97-111.

Vermote, EF, NZ Saleous, & JL Privette. 2006. Surface Reflectance Earth System Data Record/Climate Data Record White Paper. NASA, Greenbelt, MD. 6. pp.

White, MA, JD Shaw & RD Ramsey. 2005. Accuracy assessment of the vegetation continuous field tree cover product using 3954 ground plots in the south-western USA. International Journal of Remote Sensing 26:2699-2704.

Willmott, CJ 1982. Some comments on the evaluation of model performance. Bulletin of the American Meteorological Society 63:1309–1313.

Woodcock, CE, SA Macomber, M Pax-Lenney & WB Cohen. 2001. Monitoring large areas for forest change using Landsat: Generalization across space, time and Landsat sensors. Remote Sensing of Environment 78:194-203.

Woodcock, CE, SA Macomber, M Pax-Lenney & WB Cohen. 2001. Monitoring large areas for forest change using Landsat: Generalization across space, time and Landsat sensors. Remote Sensing of Environment 78:194-203.

Zhang, Q, D Devers, K Desch, CO Justice & JR Townshend. 2005. Mapping Tropical Deforestation in Central Africa. Environmental Monitoring and Assessment 101:69-83.